Measurement of Waves, Wave Groups and Wind Fields using Nautical Radar-Image Sequences

(Vom Fachbereich Geowissenschaften der Universität Hamburg im Jahr 2003 als Dissertation angenommene Arbeit)

Author:

H. Dankert

Measurement of
Waves, Wave Groups and Wind Fields
using Nautical Radar-Image Sequences

**(Vom Fachbereich Geowissenschaften der Universität Hamburg
im Jahr 2003 als Dissertation angenommene Arbeit)**

Author:

H. Dankert

(Institute for Coastal Research)

Measurement of Waves, Wave Groups and Wind Fields using Nautical Radar-Image Sequences

(Vom Fachbereich Geowissenschaften der Universität Hamburg im Jahr 2003 als Dissertation angenommene Arbeit)

Heiko Dankert

113 pages with 44 figures and 3 tables

Abstract

In this thesis, which is based on three journal papers, novel techniques are developed for retrieving individual waves, wave groups, and wind fields, spatially and temporally from nautical radar-image sequences. The images with a spatial extension of $\approx$ 4 km x 4 km and a spatial resolution of $\approx$ 10 m were recorded by the Wave Monitoring System (WaMoS), developed at GKSS Research Centre. Wave groups are derived by the first new method, based on the determination of the spatial-temporal envelope function. The wave groups are investigated regarding their spatial-temporal development, their extension and phase velocities for two sites, one in shallow water, the other one in deep water. High-resolution wind fields with a spatial resolution of up to 100 m are retrieved by the second method. The wind directions are extracted from the wind-induced streaks, which are approximately in line with the mean wind direction. The wind speeds are derived from the radar backscatter, taking into consideration the local wind direction and the air-sea surface temperature difference. The wind measurements are validated by comparing to in-situ measurements. For the investigation of single waves and wave groups an inversion scheme is introduced for determining ocean surface elevation image sequences from the radar-image sequences. This method is based on the local determination of the tilt angle of the ocean surface. The results are compared to three in-situ sensors for validation.

Messung von Wellen, Wellengruppen und Windfeldern mittels nautischer Radarbildsequenzen

Zusammenfassung

In dieser Dissertation, welche auf drei Veröffentlichungen basiert, werden neue Techniken für die raum-zeitliche Bestimmung von individuellen Wellen, Wellengruppen und Windfeldern aus nautischen Radarbildsequenzen vorgestellt. Die Bilder, mit einer räumlichen Ausdehnung von $\approx$ 4 km x 4 km und einer Auflösung von $\approx$ 10 m, wurden mit dem Wave Monitoring System (WaMoS) aufgenommen, das am GKSS-Forschungszentrum entwickelt wurde. Wellengruppen

werden mittels der ersten neuen Methode bestimmt, die auf der Berechnung der raumzeitlichen Einhüllenden beruht. Die Wellengruppen werden hinsichtlich ihrer raumzeitlicher Entwicklung, Ausbreitung und Phasengeschwindigkeiten für zwei Gebiete, eines im Flach-, das andere im Tiefwasser, untersucht. Hochauflösende Windfelder, mit einer räumlichen Auflösung von bis zu 100 m werden mit der zweiten Methode bestimmt. Die Windrichtungen werden aus den Windstreifen gewonnen, die in ungefähr in Richtung der mittleren Windrichtung an der Meeresoberfläche verlaufen. Die Windgeschwindigkeiten werden aus der Radarrückstreuung berechnet, unter Berücksichtigung der lokalen Windrichtung und der Luft-Wasser-Temperaturdifferenz. Die Windmessungen sind anhand von Vergleichen mit In-situ-Messungen validiert. Für die Untersuchung von Einzelwellen und Wellengruppen wird ein Inversionsschema zur Bestimmung von Bildsequenzen der Wasseroberfläche aus Radarbildsequenzen vorgestellt. Die Methode basiert auf der Bestimmung der lokalen Wasseroberflächenneigung. Die Ergebnisse werden mit drei In-situ-Sensoren verglichen.

Contents

List of Papers

The thesis is based on the following three journal papers:

H. Dankert, Horstmann, J., Lehner, S., and Rosenthal, W.: Detection of Wave Groups in SAR images and Radar-Image Sequences. *IEEE Transaction on Geoscience and Remote Sensing*, Vol. 41, No. 6, 2003.

H. Dankert, Horstmann, J., and Rosenthal, W.: Ocean Wind Fields Retrieved from Radar-Image Sequences. *Journal of Geophysical Research - Oceans*, Vol. 108, No. C11, doi: 10.1029/2003JC002056, 2003.

H. Dankert, and Rosenthal, W.: Ocean Surface Determination from X-Band Radar-Image Sequences. *Journal of Geophysical Research - Oceans*, submitted, 2003.

Chapter 1

Introduction

In recent years it has been demonstrated that radar images of the ocean surface provide reliable information about the spatial behavior of wave fields [*Hasselmann and Hasselmann, 1991*]. A Wave Monitoring System (WaMoS) has been developed at GKSS Research Center, Geestacht, Germany, which is in operational use [*Ziemer, 1995, Reichert et al., 1998*]. The system utilizes a common nautical X-band radar for providing time series of radar backscatter images from the ocean surface. The radar technique thereby allows measurement under most weather conditions. With the pre-existing installations of nautical radar systems at all marine structures, harbors, platforms and ships the measurements can be done in a very cost-efficient way.

Currently, it is possible to analyze these radar-image sequences regarding the retrieval of directionally unambiguous two-dimensional (2-D) image spectra *Ziemer, 1995*, a mean near-surface current vector [*Senet et al., 2001*], the mean water depth [*Outzen, 1998*], the significant wave height [*Ziemer, 1995, Borge, 1998*], and the mean wind speed for the whole measurement area [*Hatten et al., 2003*]. The WaMoS system is therefore only able to determine quantities describing the mean sea state and wind properties of an area. For estimating the significant wave height an additional calibration procedure, e.g. with a buoy, is necessary.

This thesis is based on three papers and aims at the measurement and investigation of singular waves, wave groups, and wind fields, spatially and temporally, utilizing nautical X-band radar-image sequences. The results of this thesis give mariners, offshore operators, engineers and oceanographers new opportunities for measurement and investigation of the wind and wave field conditions at and around existing maritime structures, or at and around designated areas, nearshore and off-shore, e.g. to find the best site for a construction.

The common description of the radar cross section (RCS) by *Alpers et al., 1981*, for low to moderate sea states, is in the spectral domain, as an expansion of

the spectral amplitudes, with the mean RCS and a varying part of the RCS, giving the modulation of the RCS by the ocean surface. Based on this theory and additionally by using an in-situ sensor for calibration, *Borge et al., 2003* has introduced a method for retrieving the ocean surface from radar-image sequences.

A method has been developed that allows, for the first time, analysis of the spatial and temporal properties of individual wave groups, using the retrieved ocean surface elevation image sequences [*Dankert et al., 2003a*]. This method and its ground-breaking results regarding the investigation of wave groups in space and time, e.g. their spatial-temporal development, their extension and phase velocities, are the subject of the **first paper** in chapter 3. Additionally, the method is applied to synthetic aperture radar (SAR) images for the localization of wave groups.

In the next investigative steps, it was hypothesized that the RCS is locally mainly modulated by the local wind vector and the local ocean surface. Based on this local assumption, a second method has been developed that provides, for the first time, full local information about the ocean surface wind. Method and results are published in the **second paper** in chapter 4 [*Dankert et al., 2003b*]. Further, the dependency of the RCS on the air-sea temperature difference is investigated in the paper and considered in the wind retrieval algorithm.

Further investigations have been performed, regarding the hypothesis that the RCS is locally modulated by the wind and the ocean surface. A theory has been developed based on a local description of the RCS in space and time, whereby the ocean surface is subdivided into local facets [*Wright, 1968*]. A local transfer function between the local RCS and the ocean surface is determined for each facet. The RCS is described by the geometrical effects of shadowing and tilt of the long surface waves, as well as wind. The **third paper** in chapter 5 introduces this new theory and describes an empirical inversion method based on this theory that gives, for the first time, the capability of inverting nautical radar-image sequences for determination of time series of ocean surface images without calibration [*Dankert and Rosenthal, 2003*]. The radar system can measure as a stand-alone device. Using this excellent data base, single wave properties, e.g. those of the rogue waves, can be deterministically investigated, both spatially and temporally. Further wave spectra are retrievable and, in turn, their integral spectral parameters, like the significant wave height.

The thesis is organized as follows: Chapter 2 gives for completeness, not for the general understanding of the papers, a state-of-the-art overview of measuring with WaMoS: the basic principles of the backscatter from the ocean surface, real aperture radar (RAR) imaging, the structure of the image spectra, and the retrieval of geophysical parameters. Chapters 3-5 are the three papers this thesis consists of. Finally, an outlook with suggestions for further research is given in chapter 6.

Chapter 2

Overview

2.1 The operational Wave Monitoring System

This section describes the hardware and software behind the radar system for recording and analyzing of radar-image sequences, the so-called Wave Monitoring System (WaMoS), which has been developed at GKSS research center. Several WaMoS systems are operated on an operational basis aboard towers and ships all over the world, especially in the North Sea, to measure wave parameters. The algorithms for sea state and current measurements are outlined and the limitations of the system are shown.

2.1.1 The nautical radar

Nautical radars are usually utilized for detection of targets on the ocean surface. In the open sea the radar systems normally operate at 3.0-3.1 GHz (S-band) with a far range coverage and a coarse radial resolution. In coastal areas a frequency of 9.33-9.5 GHz (X-band) is used, aiming at a high radial resolution with a smaller covered area. Because of the higher resolution, X-band devices are utilized for sea state measurements. The polarization is usually HH in transmit and receive, because for navigation purposes the radar backscatter from the sea surface is smaller then with VV polarization [*Croney, 1970*].

The nautical radar is a mono static system. The same antenna is alternately sending and receiving. The antenna is directional and radiates electromagnetic energy in patterns of lobes that extend outward from the antenna in one direction for a given antenna position. The radiation pattern also contains minor lobes, but these lobes are weak and normally have little effect on the main radiation pattern. Further, the system is pulse limited for determining the radial position of the backscattered signal by measuring the signal run time. The radial resolution

sending frequency	9375 MHz $\pm$ 30 MHz			
impulse power	25 kW			
optional setup	near range	middle range		far range
impulse duration	0.08 μs	0.3 μs	0.6 μs	1.2 μs
pulse-repeat frequency	2100 Hz	1200 Hz	1200 Hz	600 Hz
mean power	3.5 W	7.5 W	15 W	16.5 W
antenna type	4 ft / 6.5 ft open array			
horizontal directivity	1.8° / 1.23°			
vertical directivity	25° / 20°			
polarization	HH			
antenna gain	31 dB			
rotation period	2.5 s (24 rpm)			

Table 2.1: Technical data of a FURUNO X-band radar.

ρ_r is limited by the pulse duration τ. Under grazing incidence the radial resolution is given with $\rho_r = c\tau/2$, where c is the speed of light. Table 2.1 shows the technical data of the FURUNO radar system for two antenna types, which is used for sea state measurements. With a pulse duration of $\tau = 0.08$ μs the radial resolution is $\rho_r = 12$ m. The azimuthal coordinate is given from the rotating antenna position. The azimuthal resolution is retrieved from the horizontal directivity of the antenna. The directivity of an antenna refers to the degree of sharpness of its lobe, which is $\rho_\phi = 1.8°$ for the FURUNO radar system with an 4 ft antenna. The azimuthal resolution ρ_a is dependent on the distance from the antenna. At $r = 750$ m, which is about the middle range of a radar image, $\rho_a = r\rho_\phi \approx 24$ m (4 ft antenna). With a pulse repeat frequency of $f_r = 2.1$ kHz and an antenna rotation time of $\Delta t = 2.5$ s. The the azimuth angle between the radial samples is $\Delta\phi = 360°/(f_r\Delta t) = 0.068°$. The given vertical sharpness of the antenna lobe is low (for the FURUNO radar 25°) to keep the radar system independent for ship movements. Each point of a radar image is a weighted mean over the corresponding spatial-temporal resolution cell $\rho_r \otimes \rho_a \otimes \tau$.

The sending signal of a nautical radar is coherent. It consists of both amplitude- and phase-information. From the backscattered signal only the modulus of the complex signal is recorded. The phase information is not considered. The intensity of the radar backscatter from the ocean surface decreases from near range to far range with r^{-2}. The area of a resolution cell increases proportional to the distance from the radar, resulting in a received power proportional to r^{-3}. For compensation of this r^{-3} decrease, a time-dependent amplifier is operated. Additionally, at the video output of the radar system, a signal-dependent logarithmic amplifier is operated to get a larger dynamic range. A normed radar cross section of each resolution cell is not measured by a nautical radar. The measurements are done with a non-calibrated radar with incoherent receive.

2.1.2   Hard- and Software of WaMoS

The WaMoS system is provided with six input signals as shown in Table 2.2.

Source	Name	Information to WaMoS
master gyroscope	Gyro Signal	ships head relative to North
speed log	Log Signal	velocity / distance indication
radar scanner	Bearing	digital signal indicating direction of scanner at time of last transmission
scanner preamplifier	Video	pre-amplified analogue signal return from target
radar receiver	Sync	time of transmission of radar pulse
radar scanner	Heading	time of the scanner pointing in the direction of ship's head

Table 2.2: Signal inputs to WaMoS.

The WaMoS hardware provides time series of digitized radar images stored onto a mass storage medium. For typical applications, a time series of 32 image is sufficient. The contents of the digitized images are derived from the output of a digital scan converter (DSC). The DSC uses the information obtained from the Video and Sync signals to obtain the range of a received echo, and the Bearing signal to obtain the relative azimuth. This range and azimuth information is transformed to obtain X and Y offsets. The analogue output signal is sampled with a sampling frequency of, e.g. $f_{AD} = 20$ MHz, and 8 bit color depth. The sampling frequency gives a radial grid resolution of $\Delta r = c/(2f_{AD}) = 7.5$ m. The Heading marker signal is output by the radar when the scanner beam traverses from the port side to the starboard side. This increases the image counter of WaMoS. Together with the Gyro signal the ships heading relative to North and the North direction are provided. Additionally the Speed log signal gives information about the ship velocity.

The steering software of WaMoS coordinates the storage of the digitized radar-image time series and analyzes them. In the first step, the polar images are mapped onto a cartesian grid, where the grey value of each cell in the cartesian grid is given by the nearest neighbor in the polar matrix. The grid spacing of the cartesian grid is equal to the radial resolution of the polar images: $\Delta x = \Delta y = \Delta r$.

The software cuts out a rectangular part of the images and transforms this image sequence into the wave-number frequency domain using a three-dimensional Fast-Fourier Transform (3-D FFT). The wave-number $\vec{k}$ and frequency ω coordinates of the linear ocean surface waves are connected by the dispersion relation of linear surface gravity waves. The dispersion relation is, further, a function of the water depth and the velocity of encounter $\vec{u}_e$, which is a vector sum of the platform

velocity (i.e. ship) and the near-surface current $\vec{u}$. Under the assumption that the dominant part of the imaged sea state is linear and can be described with the linear theory, the dispersion relation is used as a sea state signal filter to separate signal and noise. Further, it is assumed that each wave component is sampled two times per period and no aliasing appears. With the WaMoS software up to now frequency spectra, unambiguous wave-number spectra, the significant wave height [*Ziemer, 1995, Borge, 1998*], as well as estimates of the mean near surface current velocity [*Senet et al., 2001*] and the mean water depth [*Outzen, 1998*] are determined. Further investigations have been carried out regarding the determination of high-resolution near surface current maps and the bathymetry of the measurement area [*Dankert, 2003*]. Furthermore, inversion schemes have been developed for the determination of the ocean surface from radar-image sequences [*Borge et al., 2003, Dankert and Rosenthal, 2003*] (cf. chapter 5). It is possible to study the behavior of individual wave groups in space and time [*Dankert et al., 2003a*] (cf. chapter 3). A method has been developed for the retrieval of high-resolution wind vector fields from radar-image sequences [*Dankert et al., 2003b*] (cf. chapter 4).

The WaMoS system is operationally used as a sea state warning system at certain locations at the Spanish coast [*Borge, 1995*]. Further, it is used for the measurement of sea state spectra as input for the sea state prediction model of the Norwegian Meteorological Institute, where the radar system is installed on a platform in the Norwegian oil field "Ekofisk" [*Magnusson, 1995*]. Furthermore, WaMoS is in use for the optimization of ship routes [*Ziemer et al., 1998*].

2.2   Description of investigated data

In this section all investigated data sets and the conditions at the measurement locations are described. The basis of this work are two data sets, which were operationally recorded by the company OceanWaves at two different locations. The first location is a platform of the Ekofisk oil field in the center of the North sea in a deep water area. Because of the additional in-situ sensors at this location, the data sets from this platform were used for the investigation of the retrieval of ocean wave fields from radar-image sequences. The second location is a shallow water area around the island of Helgoland in the German Bight of the North Sea.

2.2.1   Radar data from Ekofisk and Helgoland

Radar data sets from two different locations, one in deep water in the North sea, the other one in a coastal region in shallow water, have been investigated.

The deep water measurements have been carried out from the platform "2/4k" of
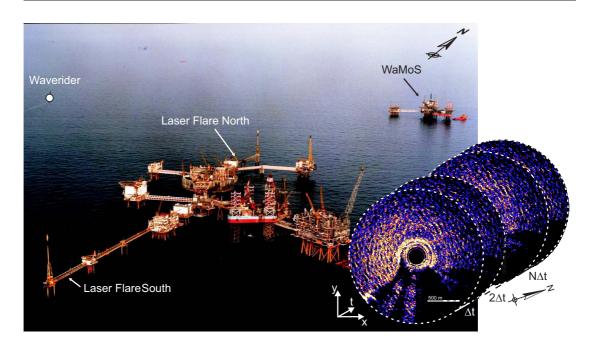
Figure 2.1: Ekofisk oil field in the North Sea operated by ConocoPhillips. The WaMoS system is installed on a platform in the background. A sample radar data set is shown.

the Ekofisk oil field operated by ConocoPhillips in the North Sea at 56.5° North and 3.2° East (Figure 2.1). The water depth in this area is about 70 m. The radar measurements in this area are operational. They are used for the determination of 2-D wave spectra and integral sea state parameters like peak wave length, peak period, and the estimation of the significant wave height in comparison to a directional wave rider buoy and two laser sensors in this area. Further, the near surface current velocity is estimated by WaMoS. The radar data are compared to collocated synthetic aperture radar (SAR) measurements.

In Figure 2.1 the platform, the location of the installed radar system and a recorded sample radar-image sequence are shown. The radar measurements are performed by a X-band FURUNO radar (Table 2.1). The radar antenna is installed at the North-West corner of the platform marked by the white arrow. The installation height of the antenna is 74 m above the mean sea level. The radar system operationally records data sets of 32 images. The time interval between two consecutive images is 2.56 s. A complete time series therefore covers a time period of ≈ 82 s. The radar-image sequence shows a wave field, which is propagating in North-East direction. The dark patches in the radar images are due to the platform equipment, e.g. the helicopter deck and the lattice towers. The higher backscatter in the south originates from the other platforms of the oilfield, which are also visible in the foreground of the photo. For the investigations, only areas representing backscatter from the sea surface are considered.
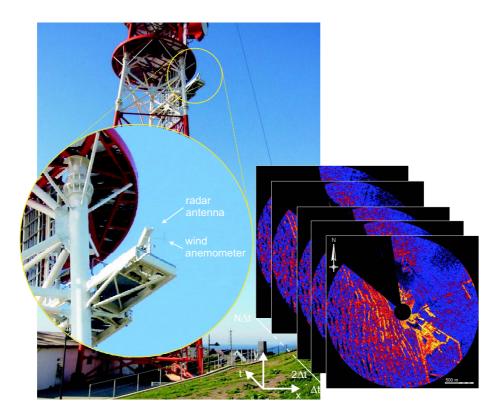
Figure 2.2: Island of Helgoland in the North Sea. The WaMoS system is installed on communication tower together with a wind anemometer.

With a sampling frequency of 20 Mhz the radial grid resolution is $\Delta r = c/(2f_{AD}) = 7.5$ m. In the near range of the antenna (0 m - 240 m) the radar signal has not reached the water surface due to the limited vertical directivity and the installation height. There is no backscatter in this so-called dead range area. The digital scan converter (DSC) is therefore delayed to detect only the radar backscatter from the end of the dead range. This area is visible in the radar image in Figure 2.1. With 256 samples in range the area covered by the antenna is from 240 m to ≈ 2160 m in radius.

Radar data sets with collocated in-situ data were available for the investigations from 02/01/2001 - 09/16/2001. The significant wave height during that period was up to 7 m. The wind speed range was up to 17 ms^{-1}

The shallow-water measurements were performed at the island of Helgoland at 54.1° North and 7.5° East in the North Sea. The average water depth here is ≈ 10 m. The radar system is also in operational use.

Figure 2.2 shows the radar antenna installed on a communication tower at a height of 90 m above the mean sea level. The Figure also shows a recorded sample radar-image sequence. The radar measurements are also performed by a X-band FURUNO radar (Table 2.1). This radar system operationally records data sets of

64 images. The time interval between two consecutive images is 1.94 s; a complete time series covers a time period of ≈ 124 s. The radar-image sequence shows an Eastern travelling wave field. Close to the coast the waves start shoaling and finally they break. The structure of the island is visible together with the harbor constructions. East of the island there are no waves because of wind shadowing due to the island and the very small fetch. The North-Western part of the images are masked out to protect the nearby lighthouse from the radar radiation. For the investigations only the area West of the island is considered.

The radial resolution is $\Delta r = c/(2f_{AD}) = 4.5$ m with a sampling frequency of 32 Mhz here. The dead range area goes from 0 m - 150 m from the image center. With 256 samples in range the area covered by the antenna is from 150 m to ≈ 1349 m in radius.

Radar data sets with collocated wind data, measured by an anemometer, were available for the investigations from 11/23/1999 - 12/02/1999. Information about significant wave heights in this area were not available, because there is no in-situ sensor installed. The maximum wind speed range was between 3 ms^{-1} and ≈ 16 ms^{-1}

2.2.2 In-situ data

From the area of the Ekofisk oil field, parallel to the radar measurements, there are wave profile measurements from 3 different sensors available as shown in Figure 2.1. The in-situ sensors are one wave rider buoy and two downwards-pointing laser sensors, one at the Northern end of the platform complex ("Flare North"), the other one at the Southern End of the complex ("Flare South"). The data are sampled continuously with 2 Hz and integrated spectral sea state parameters are extracted every 20 minutes. Additionally, there are two wind anemometers for measuring wind speed and direction installed on Ekofisk 2/4k at heights of 70 m and 116 m above mean sea level. Parallel to the wave and wind measurements the air and sea temperatures are recorded.

At Helgoland, only wind vector data from an anemometer at the height of the radar antenna were provided as shown in Figure 2.2.

2.3 Theory of real-aperture radar ocean imaging

2.3.1 Radar equation

The radar backscatter of a discrete object at a distance r from the antenna is characterized by the radar cross section (RCS) σ_0. The RCS is proportional to

the ratio of the received and the radiated energy E_r/E_t and is defined for a mono-static radar by the radar equation [*Skolnik, 1990*]:

$$\sigma_0 = \frac{E_r}{E_t} \cdot \frac{(4\pi)^3 r^4}{G_{ant}^2 \lambda_{em}^2}, \tag{2.1}$$

where G_{ant} denotes the antenna gain and λ_{em} is the wave length of the electromagnetic radiation. Regarding (2.1) the RCS is therefore range and gain independent. Normalization of the RCS to a unit area results in the normalized RCS.

2.3.2 Ocean surface scattering at grazing incidence and HH polarization

At moderate incidence angles $\Theta = 20° - 70°$ the main ocean surface scattering mechanism is Bragg scattering. The incidence angle Θ gives the angle between the perpendicular of the ocean surface and the radar beam.

Bragg scattering occurs only with a surface roughness component oriented in, or opposite to, the radar look direction, and that fulfils the Bragg resonance condition given in range and azimuth:

$$\vec{k}_{Br} = (2k_{em} \sin\Theta, 0), \tag{2.2}$$

k_{Br} denoting the resonant Bragg wave number, and k_{em} is the electromagnetic wave number [*Wright, 1966*]. The average normalized RCS (NRCS) $\sigma_{0,N}$ for HH polarization is given in the first order by [*Valenzuela, 1978*]:

$$\sigma_{0,N}^{(1)} \Theta_{HH} = 8\pi k_{em}^4 \cos^4\Theta \left| g_{HH}^{(1)}(\Theta) \right|^2 \cdot W(k_{em}, 0), \tag{2.3}$$

where W gives the two-dimensional wave amplitude power spectral density of the surface. The scattering coefficient for HH polarization is given by:

$$g_{HH}^{(1)}(\Theta) = \frac{\varepsilon_w - 1}{[\cos\Theta + (\varepsilon_w - \sin^2\Theta)^{0.5}]^2}, \tag{2.4}$$

with ε_w denoting the complex relative dielectric constant of ocean water. With the ocean surface elevation η and its slope φ parallel and δ normal to the radar look direction, the basic assumption for (2.3) is $\langle \nabla \cdot \eta^2 \rangle^{0.5} \ll 1$, with $\nabla\eta = (\varphi, \delta)$, and $k_{em}\langle \eta^2 \rangle^{0.5} \ll 1$ [*Plant and Keller, 1990*], where $\langle \cdot \rangle$ denotes the ensemble average. The assumption that the average tilt is much less than one is fulfilled in most cases.

The second condition is normally not fulfilled, because the ocean surface elevation is almost always larger than the electromagnetic wave length. The problem is overcome with the composite surface model [*Wright, 1968*]. In this, the ocean

surface is approximated with several facets having an extension that is relatively small compared to the long ocean waves, but large compared to the Bragg wave length. The Bragg scattering is applied to a co-ordinate system, where the facets are tangential to the long ocean waves, and which moves with the velocity of the long waves. For a facet with slopes φ parallel and δ normal to the radar look direction, (2.3) can be replaced by [*Valenzuela, 1978, Romeiser et al., 1997*]:

$$\sigma_{0,N}^{(1)}(\Theta, \varphi, \delta)_{HH} = 8\pi k_{em}^4 \cos^4 \tilde{\Theta} \left| \left(\frac{\sin(\Theta - \varphi)\cos\delta}{\sin\tilde{\Theta}} \right)^2 g_{HH}^{(1)}(\Theta) \right|^2 \cdot W(k_{em}, 0). \quad (2.5)$$

The local incidence angle is $\tilde{\Theta} = \arccos[cos(\Theta - \varphi)cos\delta]$, and the Bragg wave number vector $\vec{k}_{Br} = 2k_{em}[\sin(\Theta - \varphi), \cos(\Theta - \varphi)\sin\delta]$. The total NRCS of the ocean surface $\sigma_{0,N,tot}(\Theta)_{HH}$ is obtained by averaging over the local incidence angles:

$$\sigma_{0,N,tot}(\Theta)_{HH} = \int_{-\infty}^{\infty} \int_{-\infty}^{\infty} \sigma_{0,N}^{(1)}(\Theta, \varphi, \delta)_{HH} P(\tan\varphi, \tan\delta) \, d\tan\varphi \, d\tan\delta, \quad (2.6)$$

where P is the probability distribution of the slopes from the facets of a rough ocean surface. Further details on composite surface models for determination of the NRCS of the ocean surface have been developed and can be found in [*Holliday et al., 1986, Plant, 1986, Donelan and Pierson, 1987, Lyzenga and Bennett, 1988, Chen et al., 1992, Romeiser et al., 1997*].

At grazing incidence ($\Theta > 70°$) and HH polarization, as considered in this thesis, the RCS retrieved from the Bragg theory and the composite surface model is too low. *Lyzenga et al., 1983* assume wedge scattering as an important additional backscatter mechanism at grazing incidence and HH polarization. *Askari et al., 1996* have investigated the radar signatures of oceanic fronts with a X-band radar at HH polarization and grazing incidence. They come to the conclusion that the Bragg theory, and even the composite surface model, is always underestimating the RCS, and a significant part of the RCS is ascribed to small-scale breaking waves as scattering elements. *Trizna and Carlson, 1996* noted differences between horizontally (HH) and vertically (VV) polarized radar returns. The value of the RCS for VV polarization can be explained with Bragg scattering in the composite surface model, whereas spiky echoes due to breaking waves and small scale bores, induced by wave breaking, are most important for imaging at HH polarization and low grazing angles. *Wetzel, 1986* developed a bore as an idealized cylindrical feature on the front of a breaking wave as a sea spike source. *Trizna, 1997* extended this model by also considering the dielectric properties of the water surface.

Measurements of Doppler spectra of the RCS show two maxima, a fast and a slow component [*Lee et al., 1995, McLaughlin et al., 1995*]. *Lee et al., 1995* conclude that Bragg scattering at all angles relative to the wind and grazing incidence contributes to the slow peak in the Doppler spectrum. Scattering from the wave crests

vicinity (from micro-breaking and macro-breaking events) provides the energy at the fast peak.

Short capillary waves on the front of steep waves also contribute to the RCS via the Bragg mechanism, if their wave length is equal to the resonant Bragg wave length [*Longuet-Higgins, 1963, Kwoh and Lake, 1984, Gade et al., 1998*].

2.3.3   Speckle

Radar images are affected by a granular appearance, called speckle, if the roughness of the ocean surface is within the order of the electromagnetic wave length. This small-scale fluctuating component of the radar backscatter is caused by the coherent sending signal, and the interference of many (N) individual scattering elements within a radar resolution cell, analogue to the laser optic [*Goodman, 1976*]. The resulting complex scatter amplitude A is given by:

$$A = \sum_{j=1}^{N} a_j e^{i\varphi_j}, \tag{2.7}$$

where a_j is the scatter amplitude and φ_j the phase of the j-th scatter element. The phases are uniformly distributed over $[0, 2\pi]$. From the central limit theorem, it follows for a sufficient number of scatterers ($N \to \infty$) that the components of A_i ($i = \{\Re e, \Im m\}$) are Gaussian:

$$p(A_i) = \left(\pi \cdot \langle A_i^2 \rangle\right)^{-\frac{1}{2}} \cdot e^{-A_i^2/\langle A_i^2 \rangle}. \tag{2.8}$$

In an incoherent radar, like a nautical radar, the radar pulse is also coherent, but only the modulus of the complex scatter amplitude $a = |A|$ is detected, which is Raleigh distributed:

$$p(a) = 2a\langle a^2 \rangle^{-1} \cdot e^{-a^2/\langle a^2 \rangle}. \tag{2.9}$$

These considerations are for homogeneous surfaces. If the ocean surface is modulated by the sea state, the sea clutter statistic becomes non-Gaussian. Different statistical distributions have been fitted to the radar backscatter under grazing incidence [*Ward, 1988, Trizna, 1988, Sekine and Mao, 1990*]. The backscattered signal is a product of two components [*Alpers and Hasselmann, 1982*]. The first one is a temporally and spatially large scale component and is caused by modulation of the RCS by the sea state as described in the next chapter.

The second one is a temporally and spatially small-scale component, the speckle, with a de-correlation time of ≈ 10 ms. With an antenna rotation period of 2 s this signal is uncorrelated. The speckle component causes noise in the radar images. For many applications like wind vector retrieval and the ocean surface determination, which are the main concerns of this thesis, speckle is an unwanted

noise, which has to be reduced. Two methods for speckle reduction are pursued here: time-integrating over a radar-image sequence and spatial smoothing of the RCS intensities over several pixels. The first method is used for the wind field retrieval. Thereby the unwanted sea state signal is also averaged out. The spatial method is performed with a binomial filter mask (here 3×3 pixels), and is used for the determination of the ocean surface elevation at each pixel in the radar images. Otherwise the speckle signal would significantly influence the result.

2.3.4 Modulation mechanisms

The sea state is imaged by a radar, because the RCS is modulated by the long ocean surface waves. The modulation of the RCS is mathematically described by the Modulation transfer function (MTF) [*Alpers et al., 1981*], which is a sum of the four contributing processes: Shadowing, tilt modulation, hydrodynamic modulation and wind modulation. These modulation mechanisms are discussed in detail in chapter 5.

2.4 Structure of the wave-number frequency spectrum

The ocean surface elevation $\eta(\vec{r}, t)$ at a location $\vec{r} = (x, y)$ and time t can be assumed to be Gaussian, if the sea state consists of a superposition of an infinite number of spatially and temporally uncorrelated sinusoidal waves [*Phillips, 1985, Longuet-Higgins, 1963*]. Under the assumption of spatial homogeneity and temporal stationarity, the spatial-temporal wave field can be expanded after sinusoidal waves with spectral amplitudes $\hat{\eta}(\vec{k}, \omega)$, wave numbers $\vec{k} = (k_x, k_y)$, and angular frequencies ω via a three-dimensional (Fast) Fourier transform (3-D FFT):

$$\eta(\vec{r}, t) = \int_{\vec{k}} \int_{\omega} e^{i(\vec{k}\vec{r} - \omega t)} d\hat{\eta}(\vec{k}, \omega). \tag{2.10}$$

Due to the linearity of the Fourier transform the spectral amplitudes are also Gaussian and the mean is: $\langle d\hat{\eta}(\vec{k}, \omega) \rangle = 0, \forall(\vec{k}, \omega)$. The diagonal elements of the covariance matrix define the power spectrum of the wave field:

$$\mathcal{E}(\vec{k}, \omega) dk_x dk_y d\omega = \langle d\hat{\eta}(\vec{k}, \omega) d\hat{\eta}^*(\vec{k}', \omega') \rangle \qquad \forall(\vec{k}, \omega) = (\vec{k}', \omega'). \tag{2.11}$$

The non-diagonal elements are zero, and therefore spectral amplitudes with different wave-number frequency coordinates are statistically uncorrelated, giving equally distributed phases. Because $\eta(\vec{r}, t)$ is real-valued, the spectral amplitudes are hermitian $d\hat{\eta}(-\vec{k}, -\omega) = d\hat{\eta}^*(\vec{k}, \omega)$, where $\hat{\eta}^*$ denotes the complex conjugate amplitude. The power spectrum is therefore symmetric to the point of origin
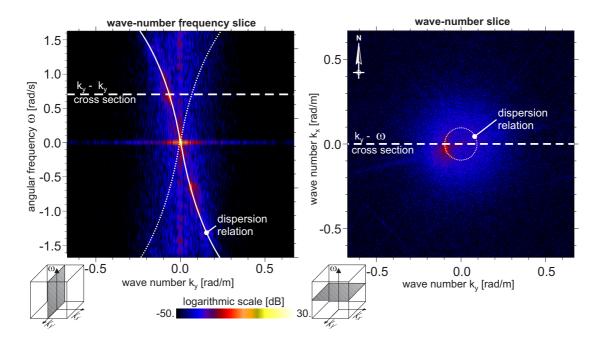
Figure 2.3: Wave-number frequency slice and wave-number slice through the 3-D wave-number frequency power spectrum of a time series of 64 radar images. The modulation signal of the see state is significantly imaged in its linear parts and located on the dispersion shell.

Radar-image sequences of the ocean surface give information about the radar backscatter from the ocean surface in grey values, and not directly the surface elevation. The considered spectra are therefore image spectra. A time series of grey-value images $G(\vec{r}, t)$ is expanded analogous to a wave field using a 3-D FFT:

$$G(\vec{r}, t) = \int_{\vec{k}} \int_{\omega} e^{i(\vec{k}\vec{r} - \omega t)} d\hat{G}(\vec{k}, \omega), \tag{2.12}$$

where $\hat{G}(\vec{k}, \omega)$ denote the spectral amplitudes of the grey values. The image spectrum $\mathcal{I}(\vec{k}, \omega)$ is defined by the diagonal elements of covariance matrix:

$$\mathcal{I}(\vec{k}, \omega) dk_x dk_y d\omega = \langle d\hat{G}(\vec{k}, \omega) dG^*(\vec{k}', \omega') \rangle \qquad \forall (\vec{k}, \omega) = (\vec{k}', \omega'). \tag{2.13}$$

The measurement duration T_{tot} and the extensions of the considered area L_x, L_y define the resolution of the spectrum: $\Delta\omega = 2\pi/T_{tot}$, $\Delta k_x = 2\pi/L_{x,tot}$, and $\Delta k_y = 2\pi/L_{y,tot}$. The Nyquist criteria define the maximum frequency and wave numbers: $\omega_{Ny} = \pi/\Delta t$, $k_{x,Ny} = \pi/\Delta x$, and $k_{y,Ny} = \pi/\Delta y$. The signal of waves with higher frequencies is convoluted into the frequency range below ω_{Ny}. Higher wave numbers cannot be acquired due to the spatial averaging. The phenomenon of frequency aliasing occurs especially for nautical radar systems operating on moving platforms or vessels. Investigation on the reconstruction of aliased spectra have been performed by *Seemann, 1997*.

Each point of the complex wave-number frequency spectrum consists of information about amplitude and phase. The phase thereby contains substantial

information about the structure of the images, whereas the amplitude indicates only that there are periodical structures in the images, but not where [*Oppenheim and Lim, 1981, Lim, 1990*]. Therefore, when a plane wave is travelling through the spatial domain, it is only shifting its phase, whereas the amplitude keeps constant. Without phase information the localization of an object in an image is not possible. The sea state signal in the 3-D image spectrum is induced by the modulation of RCS by the ocean surface waves; the background noise originates from speckle [*Goodman, 1976*]. To select the signal, the structure of the 3-D complex wave-number frequency domain has to be known. The squared amplitude of the complex 3-D image spectrum gives the so-called image power spectrum. Figure 2.3 shows example slices through an 3-D image power spectrum. The data set was recorded by a WaMoS system, installed on the island of Helgoland, and consists of 64 images. The dashed lines give the positions of the imaged cross sections. There are clearly structures visible in the spectrum that are related to the signal of the linear surface gravity waves. The signal is located on the dispersion shell, which is also indicated in the Figure and described in section 2.5.1. From the wave-number slice, information about the directional structure of the sea state can be retrieved. In the given case, a uni-modal narrow-banded wave system is travelling in Easterly direction. Further investigations on the structure of the image spectrum and its properties have been carried out by *Young et al., 1985, Seemann, 1997*.

2.5 Retrieval of geophysical parameters

In this section the relationship between the components of the image spectrum and different geophysical parameters are discussed. A new method for retrieval of high-resolution ocean current fields and bathymetries is briefly introduced. The determination of the ocean surface from the radar-image sequences, the investigation of individual wave parameters and individual wave groups belong to this section and are the main purposes of this thesis, as well as the retrieval of high-resolution wind fields.

2.5.1 Dispersion relation

Linear surface gravity waves are sinusoidal waves of infinitesimally small amplitude. For a plane wave of length L and period T the reciprocal parameters are $k = 2\pi/L$, the wave number, and $\omega = 2\pi/T$, the angular frequency, connected by the dispersion relation:

$$\varpi^2(k) = gk \tanh kd, \tag{2.14}$$

where ϖ is the intrinsic frequency, g is the gravitational acceleration and d the water depth [*Stoker, 1957*]. This function has the shape of a shell within the 3-D
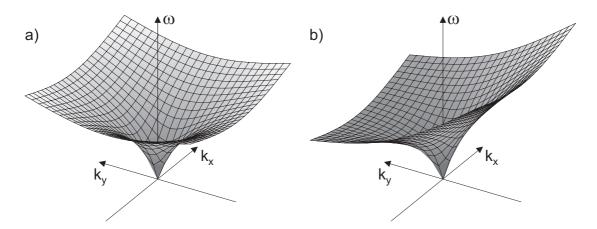
Figure 2.4: Dispersion relation for linear surface gravity waves. (a) intrinsic, (b) doppler-shifted.

wave-number frequency space as shown in Figure 2.4.

The dispersion shell is deformed by the relative movement between the sensor and the ocean surface due to the Doppler effect. The relative movement is a superposition of the near-surface current velocity and the sensor's velocity relative to the ground. Both velocities summarized give the velocity of encounter $\vec{u}_e$. *Young et al., 1985* have extended the dispersion relation by this term:

$$\omega = \varpi(k, d) + \vec{k} \cdot \vec{u}_e. \tag{2.15}$$

where ω is the angular frequency of encounter, and $\vec{k}$ the wave-number vector. Figure 2.4 shows the dispersion shell without and with doppler shift. If water depth d and velocity of encounter $\vec{u}_e$ are known, the dispersion relation is used to select the signal of the linear surface gravity waves in the wave-number frequency spectrum. Therefore, it can be used as a filter to separate this spectral part from the background noise.

2.5.2   Near surface current velocity vector and water depth

Young et al., 1985 have proposed an algorithm, based on a least-squares regression method, to determine the velocity of encounter. The theoretical dispersion shell is fitted to the signal coordinates of the linear surface waves in the 3-D spectrum. The signal coordinates are discriminated by applying a threshold to the squared modulus of the complex Fourier coefficients, the image power spectrum $\mathcal{I}(\vec{k}, \omega)$. The threshold level is typically ≈ 20 % of the power maximum. The method was improved by *Senet et al., 2001*, where temporal aliased structures in the spectrum due to the slow rotation period of the radar antenna are considered. Furthermore, nonlinear spectral structures are used to increase the number of signal coordinates for the least-squares fit. The retrieved value gives the average

direction and magnitude of the near-surface current velocity of the analyzed area. *Outzen, 1998* has extended the method by a water depth fit.

2.5.3 Sea state spectra and significant wave height

After determining water depth and velocity of encounter the dispersion relation is used as a signal filter in the image power spectrum $\mathcal{I}(\vec{k}, \omega)$ [*Ziemer, 1991*]:

$$\mathcal{I}_{sig}(\vec{k}, \omega) = \mathcal{I}(\vec{k}, \omega)\delta(\omega - \varpi^+(\vec{k}; \vec{u}_e, d)), \qquad (2.16)$$

where the delta function $\delta(\omega - \varpi^+(\vec{k}; \vec{u}_e, d))$ is the spectral bandpass filter with the dispersion relation ϖ^+ for the positive frequencies. This spectral filter separates the linear sea state signal from the background noise. By integrating over the positive frequencies of the signal-filtered power spectrum $\mathcal{I}_{sig}(\vec{k}, \omega)$ a 180° unambiguous wave-number image spectrum $\mathcal{I}^+(\vec{k})$ is determined.

$$\mathcal{I}_{sig}^+(\vec{k}) = 2 \cdot \int_{\omega_{th}}^{\infty} \mathcal{I}_{sig}(\vec{k}, \omega)d\omega, \qquad (2.17)$$

where ω_{th} is a frequency threshold to avoid energy from the static pattern.

The 180° unambiguous wave spectrum $\mathcal{E}^+(\vec{k})$ is connected with the image spectrum $\mathcal{I}_{sig}^+(\vec{k})$ by the image transfer function ITF:

$$\mathcal{I}_{sig}^+(\vec{k}) = \langle g \rangle^2 ITF(\vec{k})\mathcal{E}^+(\vec{k}), \qquad (2.18)$$

where g gives the radar backscatter and the brackets $\langle \cdot \rangle$ denote ensemble average over the large scale wave field. By this definition the ITF corresponds to the squared modulation transfer function MTF, which is often used by other authors. The ITF depends on the azimuthal angle Φ_w between the wave-propagation direction and the antenna viewing directions, with 0° looking in the wave-propagation direction [*Reichert, 1994*]. The dependency of the ITF on the modulus of the wave number $k = |\vec{k}|$ is parameterized by a power law:

$$ITF(\vec{k}) = \alpha_{ITF} \cdot \cos^2 \Phi_w \cdot k^{\beta_{ITF}}. \qquad (2.19)$$

The comparison with buoy measurements shows that a value of 1.2 for the exponent β_{ITF} is stable for a wide range of environmental conditions [*Ziemer and Rosenthal, 1993*]. The calibration constant α_{ITF} is retrieved from the empirical relationship between the signal-to-noise ratio SNR and H_S.

For radar images with non-overlapping resolution cells the speckle results in a spectral white noise floor. If the pixel size is equal to the size of the resolution cells, the spectral density of the speckle noise floor has the magnitude

$$\mathcal{I}_n^+(\vec{k}, \omega) = VAR(g)\Delta r \Delta a, \qquad (2.20)$$

with VAR(g) being the variance of the radar backscatter. For real data sets the power of the background noise can be estimated by subtracting the power of the linear sea state $\mathcal{I}_{sig}$ from the total power $\mathcal{I}$:

$$\mathcal{I}_n^+(\vec{k},\omega) = \mathcal{I}(\vec{k},\omega) - \mathcal{I}_{sig}(\vec{k},\omega), \tag{2.21}$$

With (2.18) and (2.21) the total variance of a wave field m_0 is determined from the SNR and given by

$$m_0 = V_c^2 \Delta r \Delta a \cdot \int \frac{ITF(\vec{k})^{-1}\mathcal{I}_{sig}^+(\vec{k})}{\mathcal{I}_n^+(\vec{k},\omega)} d\vec{k}d\omega, \tag{2.22}$$

with the variation coefficient V_c, which is defined as ratio between standard deviation and mean radar backscatter:

$$V_c = \frac{\sqrt{VAR(g)}}{\langle g \rangle}. \tag{2.23}$$

For a Gaussian backscattering surface the relation

$$\langle RCS \rangle^2 = VAR(g). \tag{2.24}$$

holds, and V_c is set equal to one. If the calibration coefficients and the variation coefficient are known, the significant wave height H_S is determined by:

$$H_S = 4.004 \cdot \sqrt{m_0} \tag{2.25}$$

and is deduced from the SNR. The SNR is independent of the wind field. The calibration is done by comparing radar and co-located buoy data. After the calibration the nautical radar is used as a stand-alone instrument.

Borge, 1998 has investigated and improved the described empirical correlation between SNR and H_S. He used data collected during a calibration phase by a WaMoS system installed on the Statoil operated FPSO Norne in the North Sea from November 1997 till January 1998; simultaneously, buoy measurements were carried out. The co-located buoy data sets were used for calibration of the SNR for estimation of H_S. Figure 2.5a shows a comparison of the square-root of the calibrated SNRs and the co-located H_S values from the buoy. The resultant correlation is 0.89. The improved method for determining H_S additionally takes the background noise energy on the dispersion shell into account. Figure 2.5b shows the resulting scatter plot. Comparing to Figure 2.5a gives a smaller offset in $\sqrt{SNR}$ for lower H_S values with the same correlation coefficient.
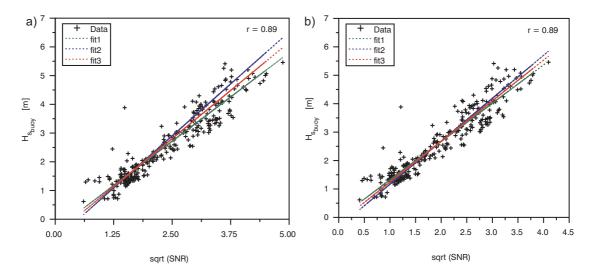
Figure 2.5: Scatterplots of $\sqrt{SNR}$ and H_S estimation by taking the wave energy and the background noise [*Nieto et al., 1998*].

2.5.4 Extension onto local spatial scale

The assumption for the standard analyzing algorithms for radar-image sequences is the homogeneity of the sea surface in the analyzed area on large spatial scales. The statistical properties within the considered region do not change. Mean hydrographic parameters are estimated for the whole analyzed area. In inhomogeneous areas, such as shallow water areas, the properties of the sea state are different at each point. Therefore several methods have been developed which can analyze radar-image sequences on a local spatial and temporal scale. *Bell, 1999* derived the shallow water bathymetry by measuring the wave celerity, which is directly dependent on the water depth (dispersion relation), using cross-correlation analysis. The resolution of the analysis technique used is limited, resulting in a limited spatial scale. The near surface currents are neglected. *Hessner et al., 2000* have introduced a method for measuring the shallow water bathymetry by using its dependency on the local wave-number (dispersion relation). The wave-number for a fixed frequency at each location is measured by determining the local phase gradient. Using the dispersion relation the bathymetry is determined. Near surface currents are neglected and directional spreading of the sea state has to be small. *Seemann et al., 1999* have developed a method for retrieving wave-number frequency spectra on a local spatial scale. Here, the dispersion relation and a directional filter select local wave-number areas with constant frequency in the wave-number frequency spectrum of the data set. After an inverse 2-D FFT complex images are given, where the phase is measured locally for retrieving a mean wave-number vector with its corresponding local magnitude. The filtering and measuring steps are applied to all areas in the spectrum containing significant energy on the dispersion relation. The filter widths are constant, therefore high

wave-numbers are spatially smeared out and low wave-numbers cannot be detected. The cuts in the spectrum cause a redistribution of energy in the spectrum and errors are introduced in the local spectra. The measurement of the phase is problematic due to noise sensitivity. Further, only the linear sea state signal is considered, whereas for moving vessels the nonlinearities are important.

Dankert, 2003 has developed a method, which is protected as an **internal GKSS patent**, that overcomes the limitations of the previously mentioned methods. Full 3-D wave-number frequency spectra, including the nonlinearities of the imaged ocean surface, are retrieved for each pixel in the analyzed area. The core of the algorithm is the Wavelet based Wave-number Frequency Selector (WWFS). The method is robust, fast and filter effects can be neglected. With the local wave-number frequency spectra high-resolution bathymetries and current fields are determined.

2.5.5   Individual Wave Parameters and Wave Groups

In contrast to the former determination of quantities describing the mean statistical properties of an area, two focal points of this thesis are investigations on the ocean surface determination and on the properties of single waves and individual wave groups. This is the subject of two of the papers in this thesis. The reader is referred to chapters 3 and 5.

2.5.6   Wind Vector

In contrast to the former estimation of the mean wind speed for a measurement area [*Hatten et al., 2003*], the measurement of high-resolution ocean wind fields is now possible with radar-image sequences, which is another main point of this thesis. The reader is referred to chapter 4.

Bibliography

Alpers, W. and Hasselmann, K. (1982). Spectral signal to clutter and thermal noise properties of ocean wave imaging synthetic aperture radars. *Int. J. Rem. Sens.*, 3, 423–446.

Alpers, W. R., Ross, D. B., and Rufenach, C. L. (1981). On the detectability of ocean surface waves by real and synthetic aperture radar. *J. Geophys. Res.*, 86, 6 481–6 498.

Askari, F., Donato, T., and Morrison, J. (1996). Detection of ocean wave fronts at low grazing angles using an x-band real aperture radar. *J. Geophys. Res.*, 101, 20 883–20 898.

Bell, P. (1999). Shallow water bathymetry derived from an analysis of x-band marine radar images of waves. *Coastal Eng.*, 37, 513–527.

Borge, J. N. (1995). First experience with the use of marine radar to survey ocean waves close to the Spanish coast. In *Proc. of the WMO/IOC workshop on operational ocean monitoring using surface based radars*, volume 32 (pp. 88–94). Geneva, Swiss.

Borge, J. N. (1998). Significant Wave Height Estimation from Nautical Radar Data Sets. In *GKSS Report 98/E/28* GKSS Research Center, Geesthacht, Germany.

Borge, J. N., Rodríguez, G., Hessner, K., and González, P. (in press 2003). Inversion of nautical radar images for surface wave analysis. *J. Atmos. and Ocean Tech.*

Chen, K., Fung, A., and Weissman, D. (1992). A backscattering model for ocean surface. *IEEE Trans. Geosci. Remote Sens.*, 30, 811–817.

Croney, J. (1970). *Radar handbook: civil marine radar*. Merril I. Skolnik.

Dankert, H. (2003). Retrieval of surface-current fields and bathymetries using radar-image sequences. *Proc. Int. Geosci. Remote Sens. Symp.*

Dankert, H., Horstmann, J., Lehner, S., and Rosenthal, W. (2003a). Detection of wave groups in SAR images and radar-image sequences. *IEEE Trans. Geosci. Remote Sens.*, 41(6), 1 437–1 446.

Dankert, H., Horstmann, J., and Rosenthal, W. (2003b). Ocean wind fields retrieved from radar-image sequences. *J. Geophys. Res.*, 108(C11, 3352, doi: 10.1029/2003JC002056).

Dankert, H. and Rosenthal, W. (submitted 2003). Ocean surface determination from x-band radar-image sequences. *J. Geophys. Res.*

Donelan, M. and Pierson, W. (1987). Radar scattering and equilibrium ranges in wind-generated waves with application to scatterometry. *J. Geophys. Res.*, 92, 4 971–5 029.

Gade, M., Alpers, W., Ermakov, S., and Lange, P. (1998). Wind wave tank measurements of bound and free propagating short gravity-capillary waves. *J. Geophys. Res.*, 103, 21 697–21 710.

Goodman, J. (1976). Some fundamental properties of speckle. *J. Opt. Soc. Am.*, 66, 1 145–1 150.

Hasselmann, K. and Hasselmann, S. (1991). On the nonlinear mapping of an ocean wave spectrum into a synthetic aperture radar image spectrum. *J. Geophys. Res.*, 96, 10 713–10 729.

Hatten, H., Seemann, J., Horstmann, J., Senet, C., and Ziemer, F. (submitted 2003). Azimuthal and range dependency of sea-surface radar backscatter at hh-polarization and low grazing incidence. *IEEE Trans. Geosci. Remote Sens.*

Hessner, K., Reichert, K., and Rosenthal, W. (2000). Mapping of sea bottom topography in shallow seas by using a nautical radar. In *Proc.*

Holliday, D., St-Cyr, G., and Woods, N. (1986). A radar ocean imaging model for small to moderate incidence angles. *Int. J. Remote Sens.*, 7, 1 809–1 834.

Kwoh, D. and Lake, B. (1984). Microwave backscattering from short gravity waves: A deterministic, coherent, and dual-polarized laboratory study of microwave backscattering from water waves, part i: Short gravity waves without wind. *IEEE J. Oceanic Eng.*, 9, 291–308.

Lee, P., Barter, J., Beach, K., Hindman, C., Lake, B., Rungaldier, H., Shelton, J., Williams, A., Lee, R., and Yuen, H. (1995). X-band microwave backscattering from ocean waves. *J. Geophys. Res.*, 100, 2 591–2 611.

Lim, J. (1990). *Two-dimensional signal and image processing*, volume 46, chapter 1.4, (pp. 35). Prentice Hall, Englewood Cliffs, New Jersey.

Longuet-Higgins, M. (1963). The generation of short capillary waves by steep gravity waves. In *J. Fluid Mech.*, volume 16 (pp. 138–159).

Lyzenga, D. and Bennett, J. (1988). Full-spectrum modeling of synthetic aperture radar internal wave signatures. *J. Geophys. Res.*, 93, 12 345–12 354.

Lyzenga, D., Maffet, A., and Shuchman, R. (1983). The contribution of wedge scattering to the radar cross section of the ocean surface. *IEEE Trans. Geos. Remote Sens.*, GE-21, 502–505.

Magnusson, A. (1995). Operational use of marine radar information in wave forecastion; status and future aspects. In *Proc. of the WMO/IOC workshop on operational ocean monitoring using surface based radars*, volume 32 (pp. 95–102). Geneva, Swiss.

McLaughlin, D., Allan, N., Twarog, E., and Trizna, D. (1995). High resolution polarimetric radar scattering measurements of low grazing angle sea clutter. *IEEE J. Oceanic Eng.*, 20, 166–178.

Oppenheim, A. and Lim, J. (1981). The importance of phase in signals. In *Proc. of the IEEE*, volume 69 (pp. 529–541).

Outzen, O. (1998). Bestimmung der Wassertiefe und der oberflächennahen Strömung mit einem nautischen Radar. In *Diploma Thesis, GKSS Report 98/E/60 (in German)* University of Hamburg, Germany.

Phillips, O. M. (1985). Spectral and statistical properties of the equilibrium range in wind-generated gravity waves. *J. Fluid Mech.*, 156, 505–531.

Plant, W. (1986). A two-scale model of short wind generated waves and scatterometry. *J. Geophys. Res.*, 91, 10 735–10 749.

Plant, W. and Keller, W. (1990). Evidence of bragg scattering in microwave Doppler spectra of sea return. *J. Geophys. Res.*, 95, 16 299–16 310.

Reichert, K. (1994). Untersuchung zur azimuthalen Abhängigkeit der Abbildung von Seegang mit dem Schiffsradar. In *Diploma Thesis, GKSS Research Center* University of Hamburg, Germany.

Reichert, K., Nieto-Borge, J., and Dittmer, J. (1998). WaMoS II: An operational wave monitoring system. In *Proc. Oceanology Int.* Brighton, U.K.

Romeiser, R., Alpers, W., and Wismann, V. (1997). An improved composite surface model for the radar backscattering cross section of the ocean surface 1. Theory of the model and optimization/validation by scatterometer data. *J. Geophys. Res.*, 102, 25 237–25 250.

Seemann, J. (1997). Interpretation der Struktur des Wellenzahl-Frequenzspektrums von Radar-Bildsequenzen des Seegangs. In *Dissertation, GKSS Report 97/E/68 (in German)* University of Hamburg, Germany.

Seemann, J., Senet, C., Dankert, H., Hatten, H., and Ziemer, F. (1999). Radar image sequence analysis of inhomogeneous water surfaces. SPIE, Proc. Conf. on "Applications of Digital Image Processing XXII".

Sekine, M. and Mao, Y. (1990). *Weibull Radar Clutter.* London, U.K.: Peter Peregrinus Ltd.

Senet, C., Seemann, J., and Ziemer, F. (2001). The near-surface current velocity determined from image sequences of the sea surface. *IEEE Trans. Geosci. Remote Sens.*, 39, 492–505.

Skolnik, M. (1990). *Radar Handbook.* McGraw-Hill, Inc., second edition edition.

Stoker, J. (1957). *Water Waves: The mathematical theory with applications*, chapter 5.5, (pp. 109–133). Interscience Publishers Inc., New York.

Trizna, D. (1988). Measurement and interpretation of north atlantic ocean marine radar sea scatter. *Naval Research Laboratory*, Report 9099.

Trizna, D. (1997). A model for brewster angle effects on sea surface illumination for sea scatter studies. *IEEE Trans. Geosci. Remote Sens.*, 35(5), 1232–1244.

Trizna, D. and Carlson, D. (1996). Studies of dual polarized low grazing angle radar sea scatter in nearshore regions. *IEEE Trans. Geosc. Remote Sens.*, 34, 747–757.

Valenzuela, G. R. (1978). Theories for the interaction of electromagnetic and oceanic waves — a review. *Boundary Layer Meteorol.*, 13, 61–85.

Ward, K. (1988). Compound representation of high resolution sea clutter. *Electron. Lett.*, 17, 561–563.

Wetzel, L. (1986). *Wave Dynamics and Radio Probing of the Ocean Surface*, chapter On microwave scattering by breaking waves, (pp. 273–284). Plenum Press.

Wright, J. W. (1966). Backscattering from capillary waves with applications to sea clutter. *IEEE Trans. Antennas Propag.*, AP-14, 749–754.

Wright, J. W. (1968). A new model for sea clutter. *IEEE Trans. Antennas Propag.*, AP-16, 217–223.

Young, I., Rosenthal, W., and Ziemer, F. (1985). A threedimensional analysis of marine radar images for the determination of ocean wave directionality and surface currents. *J. Geophys. Res.*, 90,C1, 1049–1059.

Ziemer, F. (1991). Directional spectra from shipboard navigation radar during lewex. In *in: Directional Ocean Wave Spectra, edited by R.C. Beal* (pp. 80–84). Baltimoore, U.S.A.: The Johns Hopkins University Press.

Ziemer, F. (1995). An instrument for the survey of the directionality of the ocean wave field. In *Proc. of the WMO/IOC Workshop on Oper. Ocean Mon. Using Surface Based Radars*, volume 32 (pp. 81–87). Geneva, Swiss.

Ziemer, F. and Rosenthal, W. (1993). Measurement of two-dimensional wave energy spectra during saxon-fpn'90. In *Proc. Oceans'93*, volume 1 (pp. 326–331). Victoria, Canada.

Ziemer, F., Seemann, J., and Senet, C. (1998). Measuring and predicting the forcing function for a vessel crusing in natural seas. In *Proc. of the 17th Int. Conf. Offshore Mech. and Artic Eng.* Lisboa, Portugal.

Chapter 3

Detection of Wave Groups in SAR Images and Radar-Image Sequences

Heiko Dankert[1], Jochen Horstmann[1], Susanne Lehner[2], and Wolfgang Rosenthal[1]

[1] GKSS Research Center, 21502 Geesthacht, Germany

[2] German Aerospace Center (DLR), 82234 Oberpfaffenhofen, Germany

Abstract

The properties of individual wave groups in space and time utilizing synthetic aperture radar (SAR) images and nautical radar-image sequences are studied. This is possible by the quantitative measurement and analysis of wave groups both spatially and spatial-temporally. The SAR, with its high spatial resolution and large coverage, offers a unique opportunity to study and derive wave groups. In addition to SAR images, nautical radar-image sequences allow the investigation of wave groups in space and time and therefore the measurement of parameters such as the group velocity. The detection of wave groups is based on the determination of the envelope function, which was first adopted for one-dimensional (1-D) time series by Longuet-Higgins. The method is extended from 1-D to spatial and spatio-temporal dimensions to derive wave groups in images and image sequences.

To test the algorithm, wave groups are derived from SAR images and two radar-image sequences, recorded at locations in deep and shallow water. It is demonstrated that the algorithm can be employed for the determination of both location and size of wave groups from radar images. Investigating the detected wave groups in radar-image sequences additionally allows the measurement of the spatial and temporal development of wave groups and their extension and phase velocities. Comparison of measured wave group velocities in shallow and deep water gives a deviation of the average value from the group velocities resulting from linear wave theory and shows a clear oscillation of the group velocities in 2-D.

3.1   Introduction

Wave groups play an important role for the design and assessment of offshore-platforms, breakwaters or ships, because successive large single wave crests or deep troughs can cause severe damages due to their impact, or they can excite the resonant frequencies of the structures. For ships, an encounter with wave groups can sometimes cause capsize or severe damage. An extreme wave can develop from a large wave group due to interference of its harmonic components [*Trulsen, 2001*]. Therefore the detection of wave groups in space and time is of extreme importance for ocean engineers and scientists.

In our mathematical description wave groups are the result of superposition of elementary wave components (e.g. sinusoidal waves) moving in similar direction with slightly different wave lengths and periods. The groups on the ocean surface, characterized by amplitudes above a threshold, move with their own group velocity. The group velocity is important because wave energy is propagated with this velocity. In deep water the speed of individual crests and troughs is called phase speed and is usually greater than group velocity. For a sinusoidal wave with wave number k and frequency ω the phase speed is described by $C = \omega/k$. The group velocity for a superposition of sinusoidal waves with slightly different frequencies and wave numbers is $C_g = \partial\omega/\partial k$, the gradient of the dispersion relation of linear surface-gravity waves. This mathematical idealized group velocity for a narrow spectrum is not valid for all types of observed wave groups. We will show in chapter **??** wave groups on the ocean that move with different velocities.

Wave groups have already been studied on 1d-data sets from wave recorders. Thereby the sea surface elevation is measured in situ at one fixed point over time. *Longuet-Higgins, 1957, Longuet-Higgins, 1986* was one of the first to investigate wave groups by considering the wave envelope. In this work the main assumptions are that the sea surface is considered a Gaussian process and the frequency spectrum consists of a single narrow frequency band. Only in the latter case can wave groups be meaningful defined. For a wide-banded frequency spectrum the

organized movement of waves is less noticeable and the concept of a carrier wave is not useful. Each large wave could be taken as a crest of a wave group.

The limitation of considering the sea surface over time at fixed points in space can be overcome by measuring with imaging devices. We concentrate in this work on radar images. The European satellites ERS-1, ERS-2 and recently ENVISAT, continuously record images of the ocean surface with a synthetic-aperture radar (SAR) from a near-circular, polar and sun-synchronous orbit at a mean altitude of 785 km. Thereby the radar backscatter from the ocean surface, called sea clutter, is modulated by the long surface waves. The imaging mechanisms are basically well understood [*Alpers et al., 1981, Hasselmann and Hasselmann, 1991*] so that it is possible to study the behavior of the ocean gravity waves with this instrument. The ERS-SAR acquires images with a size of approximately 100 m × 100 m with a spatial resolution of $\approx$ 25 m in range (antenna look direction) and 6 to 30 m in an azimuthal direction (flight direction). It operates at a frequency of 5.3 GHz (C-band) and transmits and receives with linear vertical polarization at incidence angles between 20° and 26°.

SAR intensity images are single images and contain no information on wave travel direction. But as in SAR images every scattering point of the sea surface is illuminated for about 0.7 seconds phase information of single look complex (SLC) data can be used to select subintervals of this integration time, creating different images of coarser spatial resolution with a time difference of about 0.5 s. By computing the cross spectrum of the two images, the direction of the wave movement can be determined [*Engen and Johnson, 1995*].

To capture a time series of ocean wave movement image sequences from a real aperture radar (RAR) can be utilized to overcome the directional limitation of single images. *Young et al., 1985* showed that it is possible to use a nautical radar to extract spectral information on the ocean surface wave field from the modulated backscatter of microwaves. For this purpose the Wave Monitoring System (WaMoS) based on a nautical radar was developed at GKSS Research Center [*Senet et al., 2001, Borge et al., 1999*], which allows for digitization of time series of polar nautical radar images. The nautical radar operates at 9.5 GHz (X-band) with horizontal and vertical polarization in transmitting and receiving near grazing incidence [*Wetzel, 1990*]. It covers an area within a radius of about 2 km. The polar images are converted to rectangular coordinates. The grid size is chosen to be equal to the radar resolution of $\approx$ 10 m. The number of analyzed radar images is basically unlimited, but 32 are sufficient for operational purposes, such as the determination of 2-D wave spectra and sea state parameters. With an antenna-rotation time of about 2 s it takes therefore about 1 minute to record a data set. Should a method exist enabling the detection of extreme wave groups in radar-image sequences, safety programs could be started before a dangerous group could reach an oil-platform. Nautical radars for wave detection are operated on several towers in the North Sea, e.g. on the Norwegian Oil Platform "Ekofisk" and in

the shallow water area at the island of Helgoland. Furthermore in the framework of the European project "MaxWave" data were recorded aboard a multipurpose container vessel sailing between Northern Europe and South Africa, passing the Aghulas Current, with strong wave-current interactions.

We emphasize in this paper the distribution and the properties of individual wave groups in space for typical sea states that are usually defined by statistical quantities like the significant wave height H_S, peak frequency f_P, directional spread etc.. An algorithm is developed and tested utilizing SAR images and nautical radar-image sequences. The wave groups from radar-image sequences are further investigated regarding their measured group velocity in comparisation with the theoretical group velocity.

3.2   Derivation of spatio-temporal wave envelope

Wave groups are the result of interference of wave components moving in similar direction with slightly different periods. The group properties of a wave record of the sea-surface elevation in time at one location can be described with its wave envelope function [*Longuet-Higgins, 1957, Rice, 1944, Rice, 1945*]. If a carrier wave can be found in the signal, the wave envelope is always defined by the local and temporal amplitude and phase. Thereby mathematically the carrier wave can always be defined as a wave with wave number $\vec{\bar{k}}$ and angular frequency $\bar{\omega}$ from the coefficients of the variance spectrum [*Longuet-Higgins, 1957*].

To retrieve 3-D wave groups (two horizontal space dimensions, one time dimension) in the spatio-temporal domain the 3-D wave envelope has to be determined. The sea-surface elevation $\eta(\vec{r}, t)$ at a location $\vec{r} = (x, y)$ and time t for a finite area of size $L_x \times L_y$ and a finite time interval T can be expressed locally as the product of a complex envelope function $\hat{\rho}(\vec{r}, t)$, the analytic signal of the real valued $\eta(\vec{r}, t)$ respectively, centered on the wave number and angular frequency of the carrier wave $(\vec{\bar{k}}, \bar{\omega})$, and a carrier wave:

$$\eta = \Re e \hat{\rho}(\vec{r}, t) e^{i(\vec{\bar{k}} \cdot \vec{r} - \bar{\omega} t)}, \tag{3.1}$$

with

$$\hat{\rho}(\vec{r}, t) = \rho(\vec{r}, t) e^{i\phi(\vec{r}, t)} = \sum_{m=-\frac{N_x}{2}}^{\frac{N_x}{2}-1} \sum_{n=-\frac{N_y}{2}}^{\frac{N_y}{2}-1} \sum_{\tau=-\frac{N_T}{2}}^{\frac{N_T}{2}-1} \xi(\vec{k}_{(m,n)}, \omega_\tau) e^{i[(\vec{k}_{(m,n)} - \vec{\bar{k}}) \cdot \vec{r} - (\omega_\tau - \bar{\omega}) \cdot t]},$$

where $k_{xm} = \frac{2\pi m}{L_x}$, $k_{yn} = \frac{2\pi n}{L_y}$ and $\omega_\tau = \frac{2\pi \tau}{T}$. $N_{(x,y)}$ are the number of points of the rows and columns in the images and N_T gives the number of images. The

wave-number vector is $\vec{k} = (k_x, k_y)$. $\hat{\rho}(\vec{r}, t)$ is defined by the wave crests, where it is determined by the wave elevation or by the square root of the potential energy E_p. The vertical velocity $w(\vec{r}, t)$ for each component is shifted relative to the amplitude by a phase of $\pi/2$. At the wave crests $\eta(\vec{r}, t)$ has its maximum and the phase $\phi = 0$. $w(\vec{r}, t)$ for each component of $\hat{\rho}(\vec{r}, t)$ vanishes at these points and therefore the kinetic energy E_k is zero. $\rho(\vec{r}, t)$ is the real envelope function of $\eta(\vec{r}, t)$, which is the modulus of the analytic function $\hat{\rho}(\vec{r}, t)$.

With the given real valued image sequence and its Fourier transform $F(\vec{k}, \omega)$, the complex envelope function $\hat{\rho}(\vec{r}, t)$ is defined by

$$
\hat{\rho}(\vec{r}, t) = 2 \sum_{m=-\frac{N_x}{2}}^{\frac{N_x}{2}-1} \sum_{n=-\frac{N_y}{2}}^{\frac{N_y}{2}-1} \sum_{\tau=0}^{\frac{N_T}{2}-1} F(\vec{k}_{(m,n)}, \omega_\tau) e^{i[\vec{k}_{(m,n)} \cdot \vec{r} - \omega_\tau \cdot t]},
$$

which is just the inverse (discrete) Fourier transform of the positive frequency part of $F(\vec{k}, \omega)$. It is likewise which frequency domain is selected since $F(\vec{k}, \omega)$ is a Hermitian function. The Fourier transform $\hat{F}(\vec{k}, \omega)$ of $\hat{\rho}(\vec{r}, t)$ is given by

$$
\hat{F}(\vec{k}, \omega) = 2u(\omega) F(\vec{k}, \omega). \tag{3.2}
$$

where $u(\omega)$ denotes the Heaviside unit step function:

$$
u(\omega) := \begin{cases} 1 & if \quad \omega > 0 \\ 0 & if \quad \omega < 0 \end{cases} \tag{3.3}
$$

To get a smoother envelope, one has to filter out the higher frequency components in the record, while on the other hand, wave components with frequencies much lower then those of the dominant waves (the mean sea surface level is generally not of interest) can be neglected. This can be done in a preprocessing step. *Longuet-Higgins, 1986* for instance filtered out the high and low frequencies. Practically, the data set is transformed into the fourier domain with a Fourier transformation and a bandpass-filter is applied to the complex Fourier coefficients for the chosen low and high cut-off frequencies.

This method for determining the envelope function can be applied to single images as well. Because of the axis dependency of the Hilbert transform in space dimensions, the elimination of the conjugate part of the Fourier coefficients in the wave-number spectrum for multi-modal wave fields can be ambiguous as the spectral peaks of the overlaying wave systems could overlap. The problem can be resolved by introducing a virtual frequency domain using the dispersion relation of linear surface-gravity waves, which is discussed later. The function is connecting the wave-number and frequency coordinates. In this way the wave-number frequency domain can be virtually constructed and the individual modes are separable.

For the time development of the sea surface elevation one may look for wave groups that propagate with a shape that is not changing in time. This means that $\hat{\rho}(\vec{r}, t)$ moves with a constant velocity $\vec{v}_G$ and has the shape

$$\hat{\rho}(\vec{r}, t) = \tilde{\rho}(\vec{r} - \vec{v}_G t). \tag{3.4}$$

$\vec{v}_G$ is not necessarily the theoretical one dimensional group velocity $\partial \omega / \partial k$.

3.3   Method for wave group detection and investigation

The scheme of the complete algorithm is described as follows and is shown in Fig. 3.1. A given record of an image sequence $G(x, y, t)$ is first transformed into the wave-number frequency domain with a 3-D Fast-Fourier Transformation (FFT), resulting in a complex 3-D image spectrum:

$$\hat{F}(k_x, k_y, \omega) = \sum_{x,y,t} G(x, y, t) e^{-i(k_x x + k_y y - \omega t)} \tag{3.5}$$

The signal of linear surface-gravity waves is well-located on a surface in the wave-number frequency domain defined by the dispersion relation of linear surface-gravity waves [*Young et al., 1985, Seemann, 1997*]:

$$\omega^2 = gk \tanh kd \tag{3.6}$$

where g is the gravitational acceleration and d the water depth. The so-called dispersion shell connects the wave-number coordinates $\vec{k}$ with their corresponding frequency coordinate ω (see also Fig. 3.2). This function is used for a pre-selection of the Fourier coefficients in the spectrum of a multimodal wave field with image features that are not resulting from ocean surface waves.

To retrieve a smooth envelope, a bandpass-filter is used to select the Fourier coefficients around the spectral peak and suppress noise from non-relevant spectral components. This is performed by a normalized 3-D Gabor filter which has the advantage of reducing the filtering effects in temporal and spatial domain. A certain wave-number range and frequency-range around the peak wave-number k_0 and peak frequency ω_0 is selected using a Gaussian function:

$$\hat{\Omega}(k_x, k_y, \omega) = e^{-\pi(|k_x - k_{x0}|^2 \sigma_{k_x} + |k_y - k_{y0}|^2 \sigma_{k_y} + |\omega - \omega_0|^2 \sigma_\omega)} \tag{3.7}$$

where σ_{k_x}, σ_{k_y} and σ_ω are the standard deviations that define the filter bandwidth in the corresponding dimensions. The filter is similar to a windowed Fourier transformation with the Gaussian function as window function. In case there are several overlapping wave systems, a segmentation has to be performed. This can
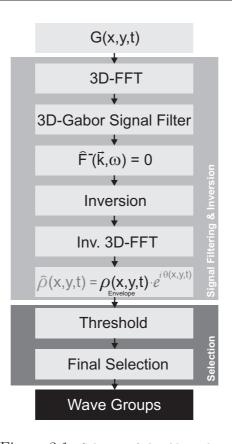
Figure 3.1: Scheme of the Algorithm.

be done in the way introduced above or by applying the 3-D Garbor filter to every significant peak in the spectrum of the dominating wave systems.

The 3-D Gabor filter is multiplied with the complex Fourier coefficients of the wave-number frequency spectrum. The remaining spectrum consists only of the dominant harmonics around the spectral peak as indicated in Fig. 3.2. To retrieve the complex envelope function of the remaining signal the complex Fourier coefficients with negative frequencies $\hat{F}^-(\vec{k}, \omega)$ are eliminated from the spectrum.

In the next step of the algorithm, an inversion technique is applied to the image spectrum $\hat{F}(\vec{k}, \omega)$ to obtain the ocean wave field [*Borge et al., 2003*]. The spectral amplitudes of the image spectrum $\mathcal{I}(\vec{k}, \omega)$ (the variance spectrum of grey levels) and the ocean wave spectrum $\mathcal{E}(\vec{k}, \omega)$ (the variance spectrum of surface heave) are connected by an image transfer function $\mathcal{M}(\vec{k})$:

$$\mathcal{I}(\vec{k}, \omega) = |\mathcal{M}(\vec{k})|^2 \mathcal{E}(\vec{k}, \omega), \tag{3.8}$$

where $\mathcal{M}(\vec{k})$ is parameterized as power law

$$|\mathcal{M}(\vec{k})|^2 = \alpha |\vec{k}|^\beta. \tag{3.9}$$
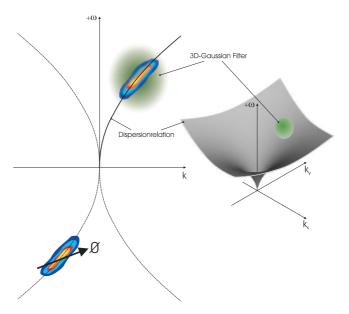
Figure 3.2: The dispersion relation is used for a pre-selection of the Fourier coefficients in the spectrum of a multimodal wave field with image features that are not resulting from ocean surface waves. After multiplying of the 3-D Gabor filter with the complex Fourier coefficients of the wave-number frequency spectrum the remaining spectrum consists only of the dominant harmonics around the spectral peak. The complex envelope function of the remaining signal is determined by eliminating the negative frequencies from the spectrum.

The exponent β has been retrieved by studying modulation effects like tilt modulation and shadowing. Thereby, *Seemann, 1997* found shadowing the dominant modulation mechanism at grazing incidence, which gives $\beta \approx 1.2$. The calibration constant α is retrieved by comparison of the spectral zero-order moment of the image spectrum with in-situ measurements of the significant wave height.

After applying a 3-D inverse Fourier transformation, the complex envelope of the wave field is determined in the spatial and temporal domain. To retrieve the dominant wave groups the modulus of the complex envelope, the amplitude, is filtered by simply thresholding. The obtained group areas are analyzed in regard to their area size, length and number of waves in a group. These parameters are used to discriminate between the groups for a final selection.

If the spectrum is wide-banded, the filtered frequency range of the bandpass filter has to be re-adjusted. The retrieved envelope will not be as smooth and maybe more difficult to analyze.
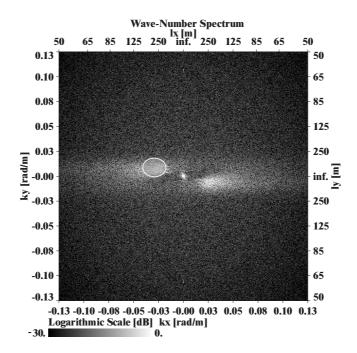
Figure 3.3: Variance of the wave-number spectrum. The complex Fourier coefficients are filtered using a 2-D Gabor filter as band-pass filter, which is indicated by the white ellipse.

3.4 Results

3.4.1 Single SAR images

Two kinds of radar images were chosen to analyze wave groups. The first is a SAR image that was acquired on September 26, 1995, at the south-west coast of Norway by the satellite ERS-1. Fig. 3.4 shows the image with dimensions of about 100 km × 100 km. In the selected sub-image, with a size of about 12.8 km × 12.8 km, a range travelling wave system is visible. The authors want to concentrate here on spatial and temporal distribution of wave envelopes and therefore the grey-level images instead of ocean topography are discussed. The nonlinearities of the SAR imaging effects such as velocity bunching and acceleration smearing are neglected [*Hasselmann and Hasselmann, 1991, Alpers and Rufenach, 1979, Krogstad, 1992*] and the authors rely on a quasi-linear approximation. The resolution of ≈30 m has the same effect as a low pass filter so that only waves longer than ≈90 m are imaged by the SAR. To retrieve wave groups, the image is processed according to the algorithm.

Fig. 3.3 shows the variance spectrum of the Fourier transformed image with range and azimuth wave numbers, k_x and k_y respectively. The corresponding wave lengths l_x and l_y are plotted on the right and top. The intensity of the spectral amplitude is normalized to the intensity of the spectral peak of the filtered wave

systems to highlight them. For retrieval of the complex envelope function, one of the point-symmetric spectral peaks is chosen using a 2-D Gabor filter, as indicated by the white ellipse in Fig. 3.3. The remaining complex Fourier coefficients are back-transformed by an inverse 2-D Fast Fourier Transform (FFT). The dominant wave groups are selected by thresholding the amplitude of the spatial determined wave envelope and by selecting only wave groups with a area size of at least $550\,\mathrm{m} \times 550\,\mathrm{m}$.

In Fig. 3.4 a SAR-sub image is depicted. Transparently overlayed are the wave envelopes of the selected dominant wave groups. A cut through the SAR image (black line in the sub image) is plotted. The thin dotted curve represents the intensity values from the SAR image, which were reduced for speckle. The band-pass filtered wave field is represented by the solid curve and the corresponding envelope function by the bold curve. Several dominant wave groups are visible. These wave groups were selected by the algorithm and marked on the envelope.

The second data set is a set of imagettes, available from the ASAR (advanced SAR) of the ENVISAT satellite launched in February 2001. The dimensions are $5\ \mathrm{km}\ \times\ 10\ \mathrm{km}$ with a pixel size of $5\ \mathrm{m}\ \times\ 20\ \mathrm{m}$. In Fig. 3.5, eight examples of the analyzed imagettes are shown. The imagettes show range travelling ocean wave fields as well as the SAR image. To retrieve wave groups the imagettes have been processed with the algorithm. The selected dominant wave groups are transparently overlayed.

The wave groups in Fig. 3.4 and 3.5 show preferred directions along which the wave groups are lined up. Their distributions in space may therefore deviate from a random selection. The wave numbers for the individual groups are well defined in components along travel directions $k_\parallel$ and perpendicular to travel direction $k_\perp$ (The authors define the travel direction perpendicular to the crest and through directions and resolve the 180° ambiguity by inspecting weather charts, which show winds from westerly directions). That means, it can be concluded quantitatively the travel speed C_g of the groups from

$$C_g = \omega/k_\parallel \tag{3.10}$$

where ω results from the deep water dispersion relation

$$\omega = g(k_\parallel^2 + k_\perp^2)^{0.5}. \tag{3.11}$$

From equation 3.10 it follows that the groups travel with the theoretical group velocity or faster, a result that will be taken up again in the following chapter.

3.4.2   Radar-Image Sequences

Using radar-image sequences the behavior of wave groups in space and time can be studied in the temporal and spatial domain. As an example the algorithm has
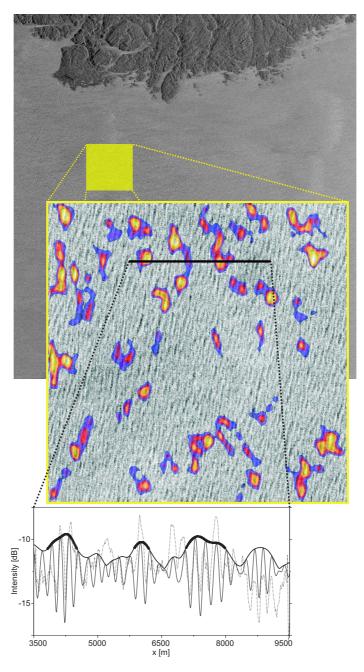
Figure 3.4: SAR image taken by the ERS-1 satellite at the south Norwegian coast on September 26, 1995. The image size is about 100 km × 100 km with a pixel size of 12.5 m. A sub image of about 12.8 km × 12.8 km has been extracted. It shows a range travelling ocean wave field. The selected dominant wave groups are transparently overlayed. A cut through the SAR image (black line in the sub image) is plotted. The thin dotted curve represents the intensity values from the SAR image, which were reduced for speckle. The band-pass filtered wave field is represented by the solid curve and the corresponding envelope function (bold curve) is overlayed. The selected groups are marked on the envelope.
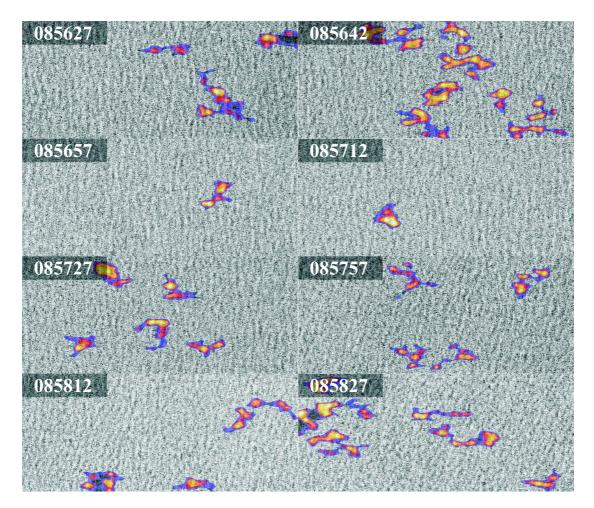
Figure 3.5: 8 Imagettes recorded by the ASAR (advanced SAR) of the ENVISAT satellite launched in February 2002. The image size is about $5\,\text{km} \times 10\,\text{km}$ with a pixel size of $5\,\text{m} \times 20\,\text{m}$. The imagettes show range travelling ocean wave fields. The selected dominant wave groups are transparently overlayed.

been applied to two radar-image sequences acquired from tower-based stations in the North sea. Both image sequences have been recorded by the Wave Monitoring System (WaMoS II). WaMoS II utilizes a conventional marine X-band radar to measure the backscatter of the microwaves from the sea surface. The temporal sampling period, given by the antenna rotation period Δt, is approximately 2 s. One data set was recorded in a shallow water area with a variable water depth of about 10 m at the island of Helgoland, the other was recorded in deep water at the Ekofisk platform. The image sequence from Helgoland consists of 64 images, whereas the Ekofisk data set has 32 images. The data sets cover a total time period of 2 minutes and 1 minute, respectively. Again, the resolution of ≈ 10 m works as a low pass filter so that only waves longer than ≈ 30 m are imaged by the system.
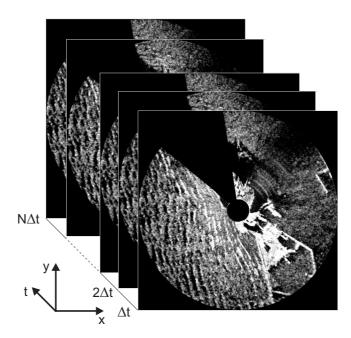
Figure 3.6: Image sequence of the radar backscatter digitized by the Wave Monitoring System (WaMoS II) at the island of Helgoland (Germany). The backscatter signal is recorded spatially and temporally. The sampling period Δt per image is approximately 2 s.

In Fig. 3.6 the image sequence from Helgoland is shown. After transforming the image sequence into the wave number-frequency domain using a 3-D FFT one gets the variance (squared modulus) and the phase of the complex Fourier coefficients. Fig. 3.7 shows a wave number-frequency slice of the variance spectrum. The signal of the linear surface gravity waves, which is located on the dispersion relation (dashed curves) is filtered by multiplying the complex spectrum with the normalized 3-D Gabor filter. Only the complex coefficients in the positive frequency domain are selected (area bounded by ellipse). The image transfer function is applied with the given significant wave height to convert the given image spectrum into a wave spectrum. After back transformation of the remaining Fourier coefficients in the wave number-frequency domain with an inverse 3-D FFT into the spatio-temporal domain, the complex envelope function of the dominant surface waves is spatially and temporally determined.

By applying a threshold on the envelope amplitude the dominant wave groups are selected. Fig. 3.8 shows the results of both analyzed cases, with the shallow water case from Helgoland (top) and the deep water case from Ekofisk (bottom). The static pattern has been removed from the images to make the imaged waves clearer. Transparently superimposed are the wave envelopes of the dominant wave groups. All the retrieved areas are counted and measured here in regard to the area size. Fig. 3.9 gives the relation between threshold level and total area size for each inverted image of the image sequence from Ekofisk. For each threshold
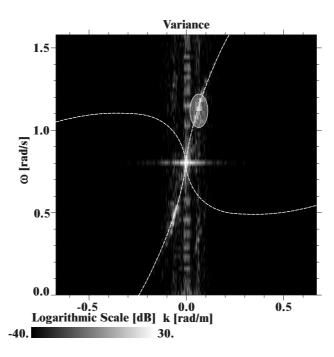
Figure 3.7: Wave number-frequency slice trough the variance of the three dimensional spectrum after applying a 3-D FFT to the image sequence. The dashed curves give the dispersion relation, whereby it's shape is changed due to near surface currents. Filtered are only the complex Fourier coefficients bounded by the ellipse. By eliminating the redundant part of the variance in the negative frequency domain the wave envelope is constructed.

level the area size is similar over the image sequence because the groups are not disintegrating in deep water due to dispersion.

The speed of wave groups, defined by the velocity at the "gravity" center of energy of the selected propagating envelope surface weighted by the potential energy ρ^2, which is termed group velocity C_g is given for one dimensional cases by:

$$C_g = \frac{1}{2}[1 + \frac{2kd}{\sinh 2kd}]C, \tag{3.12}$$

with C the phase velocity of the individual waves, which is defined as ωk^{-1}, the water depth d and wave number k. In deep water the term $(2kd)/(\sinh 2kd)$ is approximately zero, giving:

$$C_{g0} = \frac{1}{2}C \tag{3.13}$$

where the index 0 denotes deep water. In shallow water $\sinh(2kd) \approx 2kd$ and

$$C_{gs} = C \approx \sqrt{gd}, \tag{3.14}$$

with index s denoting shallow water. These equations have been used for a first comparison with the group velocities in two dimensions. The determination of velocities is done using a differential-based motion estimation technique [*Jähne et al., 1999*].

Final Selection - image = 15 Thres = 2.50 m, H$_s$ = 3.00 m, Helgoland, 12-01-1999

Final Selection - image = 8 Thres = 3.00 m, H$_s$ = 5.03 m, Ekofisk 2/4k, 02-10-2001

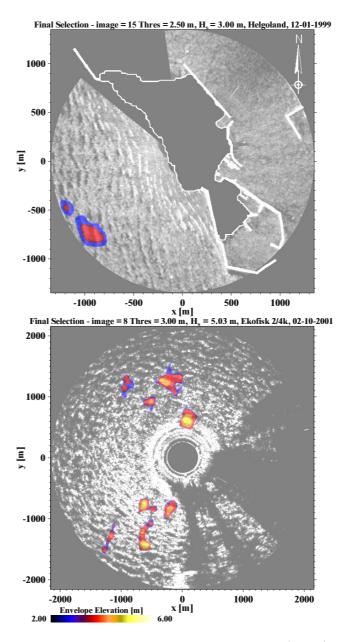**Envelope Elevation [m]**

2.00   6.00

Figure 3.8: Sample images of the image sequences from Helgoland (above) and Ekofisk (below). After applying the method one get the dominant wave groups. The static pattern has been removed from the images to make wave patterns more clear. Transparently overlayed are the wave envelopes of the dominant wave groups with a chosen minimum area size.

Fig. 3.10 shows the result for the deep water case from Ekofisk. The upper image shows the center of energy of all selected wave groups for the image sequence of Ekofisk with a threshold for wave envelope height of 3.00 m. Again, the center of energy is defined to be the "gravity" center of a wave group weighted by the potential energy ρ^2. The travel direction of all groups is varying, but goes in average with the main travel direction of the single waves. The lower plot shows
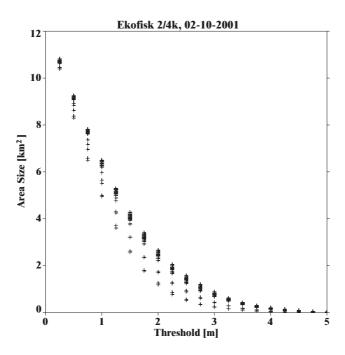
Figure 3.9: Total wave group area size for various thresholds. Each threshold is applied to all inverted envelope images of a sequence. For each threshold level the area size is similar over the image sequence because the groups are not disintegrating in deep water due to dispersion.

the phase velocity of the single waves (dashed curve) and the group velocity (solid curve) with their mean values (top) for the highlighted wave group path. The lines give the velocities regarding the linear wave theory, which are determined with the frequency and wave number at the spectral peak. Phase and group velocity are oscillating around their theoretical values. The group velocity is in average lower. In Fig. 3.11 the same plots for the shallow water case from Helgoland is shown. Theoretically phase and group velocity have the same value in shallow water. The measured average velocities are similar, but both, phase and group velocity, are oscillating over time. Sometimes the group velocity is higher, sometimes lower than the phase speed of the single waves. To give a first explanation of the physical processes behind this phenomenon one has to observe the moving single waves and the envelope function in the image sequences. Watching the animated single waves of the deep water case at Ekofisk, an observer can see waves that originate at the rear of a group, move forward through the group travelling at phase velocity and disappear at the front of the group. These waves give an explanation for seemingly increasing and decreasing group velocities. Fig. 3.12 shows a sequence of six images of the modulus of complex envelope (amplitude) from the Helgoland data set. The images have a time difference of 10 s. The dashed lines mark a distance of 500 m and the arrow gives the travel direction of the dominant group in the images. The waves in this area are travelling in an easterly direction. Observing the wave envelope gives an energy transfer in two
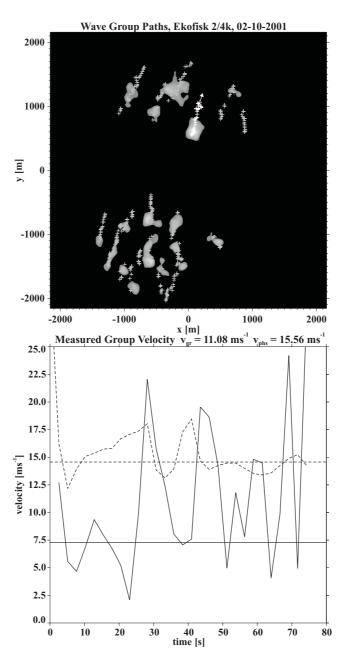
Figure 3.10: The upper image shows the center of energy of all selected wave groups for the image sequence of Ekofisk with a threshold for wave envelope height of 3.00 m (white area). The center of energy is defined to be the "gravity" center of a wave group weighted by the potential energy ρ^2. The travel direction of all groups is varying, but goes in average with the main travel direction of the single waves. The lower plot shows the phase velocity of the single waves (dashed curve) and the group velocity (solid curve) with their mean values (top) for the highlighted wave group path. The lines give the velocities regarding the linear wave theory.

dimensions and therefore also addresses the wave crests. Determining the angle of the measured group-velocity vector validates the observation and shows that wave

Wave Group Paths, Helgoland, 12-01-1999

Measured Group Velocity $v_{gr} = 8.35$ ms^{-1} $v_{phs} = 11.26$ ms^{-1}
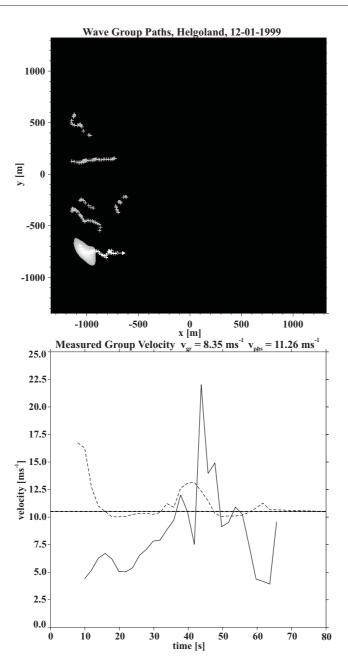
Figure 3.11: The images show the same like Fig. 3.10 for the image sequence of Helgoland in a shallow water area with a threshold for wave envelope height of 2.50 m (white area). The travel direction of the groups is particulary strongly varying, but goes in average with the main travel direction of the single waves.

groups are, therefore, not only travelling with the waves. Furthermore, one can see how the wave group is developing and is varying in both amplitude and horizontal dimensions. A transversal modulation of the wave groups by other waves systems might be an explanation. The 2-D change in size of the wave groups is especially
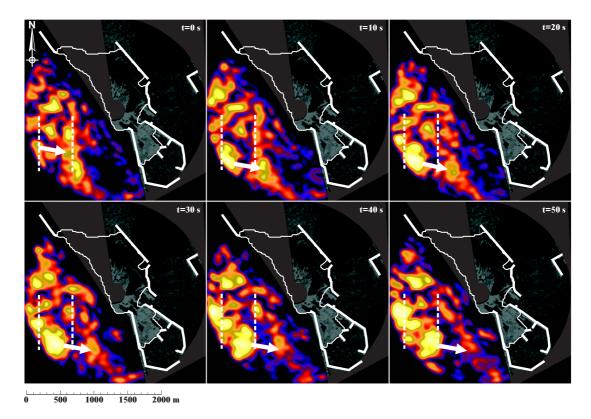
Figure 3.12: Sequence of six images from Helgoland of the modulus of the complex envelope function after applying a inverse 3-D FFT to the filtered complex Fourier coefficients of the wave number-frequency spectrum. The images have a time difference of 10 s. The dashed lines mark a distance of 500 m and the arrow gives the travel direction of the dominant group in the images.

interesting because it may be correlated with the background horizontal currents in the area [*Dysthe, 2001*].

3.5 Summary

Properties of individual wave groups in single radar images as well as radar-image sequences have been studied. This was possible by the quantitative measurement and analysis of wave groups both spatially and spatial-temporally. An image or image sequence of linear surface gravity waves is band-pass filtered and the temporal envelope was defined at each point. The filtering and determination of the complex envelope function are performed in the Fourier domain. The radar-image sequences are inverted to give the 2-D sea-surface elevation. The retrieved groups are investigated with regard to their area size and maximum amplitude.

A SAR image acquired by the European satellite ERS-1, imagettes from the Eu-

ropean satellite ENVISAT and image sequences recorded using a conventional nautical radar have been analyzed. The SAR image has been recorded at the south-west coast of Norway and the ENVISAT imagettes are first examples from the ocean surface. The radar-image sequences are from two different locations, one from a shallow water area at the island of Helgoland and the other one from a deep water area at the Ekofisk platform. It was possible to determine location and size of wave groups from SAR imagery. The large coverage of SAR images, together with their high resolution, provide valuable information about the distribution and size of wave groups. Radar-image sequences, collected with the WaMoS system, allow the measurement of the spatial and temporal development of wave groups, their extension and velocities, which has been done here. Comparison of measured wave group velocities in shallow and deep water gives an agreement of the average value with the group velocities resulting from linear wave theory and shows a clear oscillation of the group velocities in 2-D.

Overall, the application of the algorithm on SAR images and the results from nautical radar-image sequences show the applicability of these data for detection and measuring of wave groups in spatial and temporal dimensions.

In the next step the physics behind the phenomenon of oscillating group velocity and energy transfer along the wave crest is further investigated.

Acknowledgements

Bibliography

Alpers, W. R., Ross, D. B., and Rufenach, C. L. (1981). On the detectability of ocean surface waves by real and synthetic aperture radar. *J. Geophys. Res.*, 86, 6 481–6 498.

Alpers, W. R. and Rufenach, C. L. (1979). The effect of orbital motions on synthetic aperture radar imagery of ocean waves. *IEEE Trans. Antennas Propagat.*, 27, 685–690.

Borge, J. N., Hessner, K., and Reichert, K. (1999). Estimation of the significant wave height with x-band nautical radars. In *Proc. 18th Intern. Conf. on Offshore Mech. and Arctic Eng. (OMAE)*, number OMAE99/OSU-3063 St. John's, Newfoundland, Canada.

Borge, J. N., Rodríguez, G., Hessner, K., and González, P. (in press 2003). Inversion of nautical radar images for surface wave analysis. *J. Atmos. and Ocean Tech.*

Dysthe, K. (2001). Refraction of gravity wave by weak current gradients. *J. Fluid. Mech.*, 442, 157–159.

Engen, G. and Johnson, H. (1995). SAR-ocean wave inversion using image cross spectra. *IEEE Trans. Geosci. Rem. Sens.*, 33, 1047–1056.

Hasselmann, K. and Hasselmann, S. (1991). On the nonlinear mapping of an ocean wave spectrum into a synthetic aperture radar image spectrum. *J. Geophys. Res.*, 96, 10 713–10 729.

Jähne, B., Haußecker, H., and Geißler, P. (1999). *Handbook of Computer Vision and Applications*. Academic Press.

Krogstad, H. (1992). A simple derivation of Hasselmann's nonlinear ocean-synthetic aperture radar transform. *J. Geophys. Res.*, 97, 2 421–2 425.

Longuet-Higgins, M. (1957). The statistical analysis of a random moving surface. In *Phil. Trans. R. Soc. London A* (pp. 321–387).

Longuet-Higgins, M. (1986). Wave group statistics. In *E.C. Monahan and G. Mac Nioceill (eds.), Oceanic Whitecaps* (pp. 15–35).

Rice, S. (1944). The mathematical analysis of random noise. In *Bell Systems Technical Journal*, volume 23 (pp. 282–332).

Rice, S. (1945). The mathematical analysis of random noise. In *Bell Systems Technical Journal*, volume 24 (pp. 46–156).

Seemann, J. (1997). Interpretation der Struktur des Wellenzahl-Frequenzspektrums von Radar-Bildsequenzen des Seegangs. In *Dissertation, GKSS Report 97/E/68 (in German)* University of Hamburg, Germany.

Senet, C., Seemann, J., and Ziemer, F. (2001). The near-surface current velocity determined from image sequences of the sea surface. *IEEE Trans. Geosci. Remote Sens.*, 39, 492–505.

Trulsen, K. (2001). Simulating the spatial evolution of a measured time series of a freak wave. In *Proc. Rogue Waves 2000* (pp. 265–273). Oslo, Norway.

Wetzel, L. (1990). Electromagnetic scattering from the sea at low grazing angles. *Surface Waves and Fluxes, Geernaert and W.J. Plant (eds.), Kluwer Academic Publishers*, II, 109–171.

Young, I., Rosenthal, W., and Ziemer, F. (1985). A threedimensional analysis of marine radar images for the determination of ocean wave directionality and surface currents. *J. Geophys. Res.*, 90,C1, 1049–1059.

Chapter 4

Ocean Wind Fields Retrieved from Radar-Image Sequences

Heiko Dankert, Jochen Horstmann, and Wolfgang Rosenthal

GKSS Research Center, 21502 Geesthacht, Germany

Abstract

The dependency of radar backscatter on the surface wind field is investigated using a nautical X-band radar operating at grazing incidence and horizontal polarization in transmit and receive. This resulted in development of an algorithm for wind retrieval from nautical radar image sequences. The algorithm consists of two parts: In the first part, wind directions are extracted from wind induced streaks that are in line with the mean surface wind direction. These streaks are visible in the temporal integrated radar images at scales between 100 and 500 m. The orientation of the streaks is determined from the local gradients, which are derived from the radar images smoothed and reduced to the appropriate scales. In the second part, wind speeds are derived from the backscatter of the temporal integrated radar image sequence and the radar retrieved wind direction. The dependency of the radar backscatter on the local surface wind and geometry of the radar is parameterized by training a Neural Network. The algorithm is applied to radar image sequences acquired by a nautical X-band radar mounted aboard an offshore platform in the North Sea. The radar derived winds are validated by comparison to in-situ wind data measured at the platform. The com-

parison of wind directions resulted in a correlation of 0.99 with a standard deviation of 14.2° for wind speeds the correlation is 0.97 with a standard deviation of 0.85 ms⁻¹. In contrast to traditional offshore wind sensors, the retrieval of the wind field from the backscatter of the ocean surface makes the system independent of the sensors motion and installation height and reduces the effects due to platform induced blockage and turbulence effects.

4.1   Introduction

Wind is a major driving force in ocean dynamics; it is responsible for the transfer of energy and momentum from the atmosphere to the ocean and supports the gas-exchange processes between the lower marine atmospheric boundary layer and upper ocean surface. Thus wind is a key parameter in the coupled atmosphere, ocean and biosphere system. Measurements of ocean winds are performed using various different methods, e.g. in-situ by anemometers (point measurements through time), and by remote sensing with scatterometers (spatial measurements). In situ measurements are mainly collected by ships and buoys of which the first are affected by blockage effects and variable mast heights and the latter by tilt and displacement height, especially in high winds and sea states. The remote sensing techniques require excellent calibration as well as model functions that parameterize the dependence of the backscatter on the wind and have a rather coarse resolution.

In this paper a radar based remote sensing technique is introduced, which enables the measurement of the ocean surface wind from towers and ships. Therefore a nautical radar operating at X-band is used that has the capability of measuring the backscatter from the ocean surface in space and time under most weather conditions, independent of light conditions. Biases of wind measurements, due to tilt and height variation, as well as due to the sensor motion, do not exist. Also, the blockage, as well as the turbulence effects due to the sensor platform, are strongly reduced and, in case of tower based measurements, are considered in the algorithm.

In addition to the wind retrieval presented here, nautical radar image sequences of the sea surface are also used to determine other hydrographic parameters. In particular they have been used to determine: two-dimensional wave-spectra and significant wave heights [*Borge et al., 1999*], individual wave parameters [*Borge et al., 2003*], wave groups [*Dankert et al., 2003a*], the near surface current [*Senet et al., 2001*], and bathymetry [*Bell, 1999, Trizna, 2001*]. Recently, new methods for the current and bathymetry field retrieval from the nautical radar image sequences have been developed [*Dankert, 2003*].

It is well known that the local wind field generates the small-scale roughness of the sea surface, which in turn raises the radar backscatter of the ocean surface

[*Lee et al., 1995, Trizna, 1997*]. The radar cross section (RCS) of the sea surface is strongly dependent on the local wind speed [*Lee et al., 1996*] and angle between the antenna viewing direction and wind direction [*Hatten et al., 2003*]. This dependency enables the deduction of the wind vector from radar images of the sea surface. In the presence of long surface waves, the small-scale surface roughness, and subsequently the radar backscatter, is modulated. At moderate incidence angles the modulation is mainly due to the tilt and hydrodynamic modulation [*Alpers et al., 1981*], while at grazing incidence the modulation stems also from the shadowing of the radar beam due to the ocean waves [*Wetzel, 1990*]. These modulation mechanisms lead to the imaging of surface waves whose wavelength are greater than two times the radar resolution.

Several studies on the wind dependency of radar data acquired at grazing incidence have already been performed [*Chaudhry and Moore, 1984, Lee et al., 1996, Hatten et al., 2003*]. In these studies the dependency of the RCS on wind speed and direction has been investigated. *Hatten et al., 2003* showed that the spectral noise of X-band HH-polarized radar images is correlated with the wind speed and wind direction. *Keller et al., 1985* have studied the dependency of the RCS on air-sea temperature difference and sea state [*Keller et al., 1994*]. For a detailed description of scattering at low grazing incidence refer to *Wetzel, 1995* and *Brown, 1998*.

In this paper a new algorithm is proposed to retrieve ocean winds from nautical radar-image sequences. The algorithm consists of two parts, in the first, wind directions are retrieved from wind-induced streaks, which are imaged by the radar at scales of approximately 100 to 500 m, using a method based on derivation of local gradients [*Horstmann et al., 2002, Koch, 2003*]. This method has already been successfully applied for wind direction retrieval from space borne synthetic aperture radar (SAR) images [*Horstmann et al., 2002*]. In the second part, the dependency of the RCS on wind is parameterized by training a Neural Network (NN). NNs have been used in several applications in remote sensing, e.g., derivation of water properties from imaging spectrometers [*Schiller and Doerffer, 1999*], as well as for wind retrieval from scatterometer (SCAT) [*Richaume et al., 2000*] and SAR data [*Horstmann et al., 2003*]. In addition to the wind dependency of the RCS, the dependency on the air-sea temperature difference is considered in the wind retrieval algorithm.

The paper is organized as follows: In Section 5.2 the radar system and available data are introduced. Section 4.3 shows the dependency of the radar image intensity on wind speed and direction. In Section 4.4 the wind direction retrieval algorithm is introduced and applied to the radar data sets. The determined wind directions are compared to in-situ data recorded at the radar platform. In Section 4.5 NNs are introduced and applied to wind speed retrieval from the radar-image sequences. The radar retrieved wind speeds are compared to the in-situ measurements collected at the platform. Finally, in Section 5.6, conclusions and an

outlook are given.

4.2   Investigated data

The utilized radar system consists of a typical nautical radar and a WaMoS II unit, which allows for the continuous digitization of time series of polar nautical radar images. The nautical radar was operated at 9.5 GHz (X-band) with horizontal (HH) polarization in transmit and receive at grazing incidence in a height of 74 m over mean sea level. For wind retrieval the radar covers an area within a radius of ≈ 2000 m with a antenna-revolution time of ≈ 2.5 s. The spatial resolution at a distance of ≈ 750 m from the antenna is ≈ 10 m in range and ≈ 12 m in azimuth. Several WaMoS II systems are operated on an operational basis aboard towers and ships in the North Sea to measure wave parameters. However, the 4 months of investigation of radar-image sequences from February to June 2001, representing 3271 acquisition times, were recorded at the Norwegian platform Ekofisk 2/4 k located ≈ 200 km off the west coast of Norway in the North Sea. Each image sequence consists of 32 images, representing a time span of ≈ 80 s.

Nautical radar systems are equipped with a logarithmic amplifier and are not radiometrically calibrated. Therefore, the normalized RCS could not be determined. The backscattered signal of each radar resolution cell is digitized with 8 bit, which allows grey values between 0 (no backscatter) and 255 (highest signal).

In Fig. 5.1, the platform, the location of the installed radar system and a recorded sample radar-image sequence are shown. The radar antenna is installed at the North-West corner of the platform marked by the white arrow. The radar-image sequence shows a wave field, which is propagating in north-east direction. The dark patches in the radar images are due to the platform equipment, e.g. the helicopter deck and the lattice towers. The higher backscatter in the south originates from the other platforms of the oilfield, which are also visible in the background of the photo. For the investigations, only areas representing backscatter from the sea surface are considered. The range-ring patterns in the near range are caused by multiple reflections of the antenna side lobes in the near-field from the host platform equipment in a distance of about 500m, due to the longer running time of the radiated energy. To neglect this effect the investigations have been performed beginning at 900 m range.

For comparison wind measurements were collected by a wind anemometer and a wind vane, mounted at a height of 80 m above sea level at Ekofisk 2/4 k. The in-situ wind speeds are 10 minutes means and are converted to 10 m height. In addition the air- and water temperature as well as significant wave heights and peak periods were collected at Ekofisk 2/4 k with a wave rider buoy beside the platform.
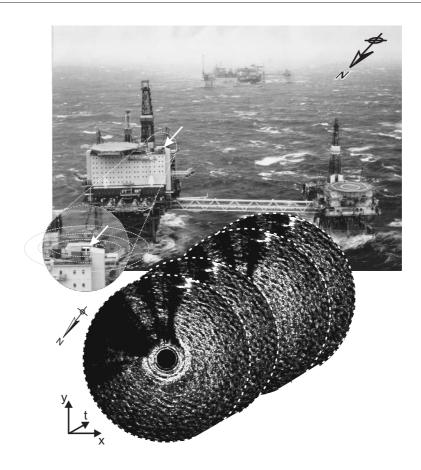
Figure 4.1: Ekofisk 2/4 k platform of the Ekofisk oil field in the North Sea. The WaMoS system is installed at the north-west corner of the platform. In the radar images several shadows are visible, which are due to the equipment of the platform. The large backscatter in the south originates from the oil field visible in the background of the photo.

4.3   Wind dependence on the radar cross section

It is well known that the backscatter of the ocean surface is primarily caused by the small-scale surface roughness, which is strongly influenced by the local wind field and therefore allows the backscatter to be empirically related to wind. Measurements at grazing incidence indicate that the backscatter at grazing incidence with HH polarization results from small scale breaking waves as scattering elements [*Lee et al., 1995, Wetzel, 1995, Trizna, 1997, Brown, 1998*]. The RCS of the ocean surface, σ, is related to the near-surface wind speed u and antenna-look direction versus wind direction, $\Delta\Phi = \Phi_{radar} - \Phi_{wind}$:

$$RCS = a \cdot u^{\gamma}(1 + b \cdot \cos\Delta\Phi), \tag{4.1}$$

whereas $\Delta\Phi$ is defined here as 180° looking up-wind. The coefficients a, b and γ generally depend on radar frequency, polarization and incidence angle.

By integrating a radar-image sequence over time (typically 32 images representing
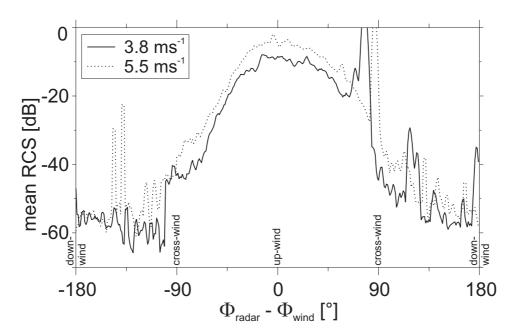
Figure 4.2: Wind direction in respect to radar look direction versus range-integrated RCS for different wind speeds. The data were acquired from a tower based radar in the Odra Lagoon at the German coast of the Baltic Sea.

1 min of data), signatures with higher variability in time (like surface waves) are averaged out. Only static patterns such as the shadows from the towers and the wind signatures remain visible in the mean RCS $\bar{\sigma}$. The hypothesis is, $\bar{\sigma}$ depends on the wind direction and wind speed, whereas the temporal and spatial variability of the backscatter distribution is mainly due to the local wave field modulation. Both processes show an azimuthal dependency.

In Fig. 4.2 the wind direction, with respect to the radar look direction, is plotted versus the mean RCS in range for a wind speed of 3.8 and 5.5 ms^{-1}. The radar image sequences were acquired by a similar radar system installed in the Odra lagoon at the German coast of the Baltic Sea in summer 1997. In this setup the radar images were not affected by shadows caused by equipment. Furthermore, the RCS was not modulated by ocean waves, due to the very limited fetch and very shallow water depth in this area. The two curves show that the RCS has its maximum when the antenna is viewing in up-wind direction ($\Delta\Phi = 0°$) and has a minimum when viewing in down-wind direction ($\Delta\Phi = \pm180°$). This result for X-band with HH polarization is in accordance with results of *Trizna and Carlson, 1996* and *Hatten et al., 2003*. The single peak stands in contrast to radar measurements of the sea surface in X-band with VV polarization and radars operating at moderate incidence angles where two maxima are observed, one at up-wind and one at down-wind [*Trizna and Carlson, 1996,* **?**]. Local minima are here at cross-wind. The up-wind RCS is slightly higher than the down-wind one. The single peak makes radar measurements obtained with HH polarization at grazing incidence the best choice for wind direction measurements, because they enable
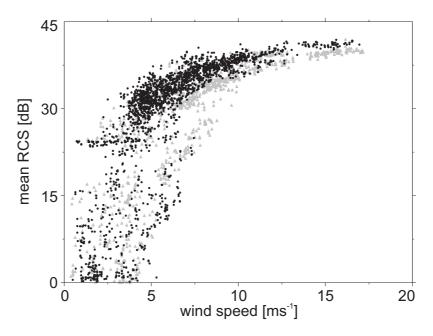
Figure 4.3: Scatter plot of in situ wind speed versus mean RCS. Solid dots represent mean RCS from data sets acquired at wind directions between 170° and 40°, while grey triangle represent data between 40° and 170°.

the retrieval of unambiguous wind directions (refer to Section 4.4).

Fig. 4.3 shows the scatter plot of in situ wind speeds converted to 10 m height versus mean RCS of each of the radar image sequences. The mean RCS was retrieved from the total image sequence excluding the masked area shown in Fig. 4.4. There is a strong dependency of the mean RCS on wind speeds over the entire range of wind speeds. A group of outliers (grey triangles) can be identified with a shift of the RCS toward lower intensities. These outliers belong to radar sequences where the wind direction was between 40° and 170°. In these cases the upwind peak of radar backscatter is expected to be located in the masked area, which was neglected in retrieval of the mean RCS and therefore leads to a lower mean RCS than expected.

4.4 Wind direction retrieval

The wind direction retrieval is based on wind-induced streaks, which are visible in the mean radar image resulting from integration of the radar-image sequence over time.

The wind induced streaks are aligned in wind direction and have a typical spacing of 100 to 500 m. They are most likely caused by features such as local turbulences, streaks from foam or surfractants that are aligned with the mean surface wind direction. Wind induced streaks have also been observed in satellite borne SAR im-
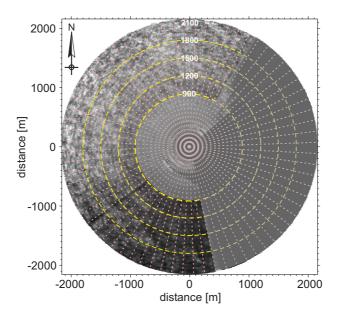
Figure 4.4: Mean RCS of a radar-image sequence of 32 images from Ekofisk 2/4 k. The masked area was not considered for the wind retrieval. The polar image is divided into subareas in range (300 m) and azimuth (5°).

agery at similar [*Horstmann et al., 2002*] and larger scales [*Gerling, 1986*] and are used to retrieve the wind direction [*Lehner et al., 1998, Horstmann et al., 2002, Wackerman et al., 2003*]. In the following, wind-induced streaks are assumed to be approximately in line with the mean wind direction.

The orientation of wind-induced streaks is normal to the local gradients derived from smoothed amplitude images. To retrieve the local gradients, the mean RCS image is iteratively smoothed and sub-sampled to obtain a so-called Gaussian pyramid. From level to level the resolution decreases by a factor of two; the RCS image size decreases correspondingly to a pixel size of 20, 40 and 80 m. From these pixels the local directions are computed with a 180° directional ambiguity. The wind directions resulting from the different pixel sizes vary typically only by a few degrees, except for cases were additional features are present. A detailed description of the local gradient based algorithm for retrieval of wind induced streaks is given by [*Koch, 2003*].

In principle, the 180° directional ambiguity could be removed searching for the upwind peak in the mean polar image (see Fig. 4.2). However, most radar installations do not allow the recording of the backscatter from the ocean surface over the entire azimuth (entire revolution of antenna). Often the radar is affected by platform equipment that lead to disturbed areas in the polar radar image (fig. 5.1) and therefore in difficulties finding the upwind peak. This is especially the case for radar systems based at the coast as well as for systems aboard oil rigs such as the setup of Ekofisk 2/4k.
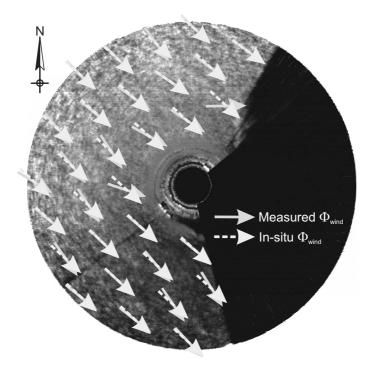
Figure 4.5: Mean RCS of a radar-image sequence from Ekofisk 2/4 k on April, 15th 2001. The wind speed was 8 ms^{-1} and the measured wind direction at 74 m height (dashed arrows) 335°. Superimposed are solid arrows giving the retrieved local wind direction at the ocean surface.

In this case the 180° directional ambiguity is removed by extracting the movement of wind gusts visible in the radar image sequence. The radar image sequence is subdivided into two or more sub-sequences (typically 24 images), which may overlap each other in time. Each subsequence is then integrated over time to remove signatures with higher temporal variability such as ocean surface waves. From these mean RCS images the movement of wind gusts is retrieved. A standard technique to estimate the shift of moving image patterns between two data takes is to compute the cross-correlation function (CCF). The respective propagation distance is indicated by the location of the CCF peak. Alternatively the shift can also be estimated looking at the cross spectrum (CS), which is defined as the Fourier spectrum of the CCF. In the CS the shift of the different harmonic waves in the image is given by the respective phases of the complex valued CS. The directions resulting from the CS are always within 90° of the in situ measured wind direction and therefore enables the 180° directional ambiguity left open by the local gradient method to be resolved. The same results can be achieved using differential-based motion estimation techniques [*Jähne et al., 1999*], which enable the retrieval of the movement of the mean RCS at each pixel [*Dankert et al., 2003b*]. Also in this case the mean resulting direction is within 90° of the in situ measured wind direction. However, the latter method requires significantly longer computation times.
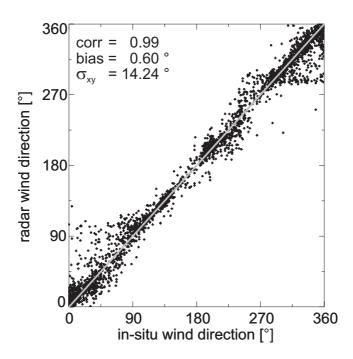
Figure 4.6: Scatterplot of in-situ wind directions versus radar-derived wind directions.

In Fig. 4.5 the mean RCS image resulting from the image sequence is shown. Superimposed onto the radar image are the wind directions resulting from the 240 m pixel layer of the local gradient retrieval scheme (solid line arrows) and the in situ measurements (dashed line arrows). It can be seen that both measurements agree well.

In Fig. 4.6 the scatter plot of the comparison of wind directions measured in situ and by the radar system is given. In this case the radar wind direction for each measurement represents the mean of all determined local wind directions. The scatter plot considers all of the 3271 image sequences. The standard statistical parameters result in a correlation of 0.99 a bias of 0.6° and a standard deviation of 14°.

In Fig. 4.7 wind speed is plotted versus wind direction differences resulting from radar and in situ wind directions. Superimposed are the bias (solid line) and standard deviation (dotted line) in dependence on wind speed. The dependence of the bias on wind speed is negligible, however, the standard deviation decreases significantly with increasing wind speed.

Slightly larger errors were obtained from satellite borne SAR imagery, were wind directions were retrieved from streaks at scales above 400 m and compared to in situ measurements [*Vachon and Dobson, 1996, Lehner et al., 1998, Fetterer et al., 1998*] as well as to numerical model results [*Horstmann et al., 2002*]. The comparison of SAR derived wind directions retrieved at different scales [*Wackerman et al., 2003*] indicate that the smaller
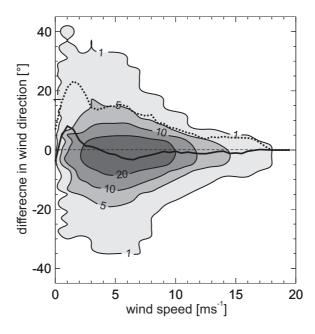
Figure 4.7: Scatterplot of wind speeds versus difference between radar and in-situ wind directions. The solid and dotted line give the bias and standard deviation respectively.

scales used here are better suited for wind direction retrieval.

4.5 Wind speed retrieval using Neural Networks

A straightforward method for retrieving wind speeds from uncalibrated radar images can be obtained by using a NN. The NN approach does not require explicit models for the radar imaging process and can therefore be easily applied to any system configuration, i.e. polarization, incidence angle e.t.c.. The only requirements for application of a NN to radar-wind-speed retrieval is the relative radiometric stability of the system as well as a dependency of backscatter on wind speed. In the case of the system aboard Ekofisk 2/4k both requirement are fulfilled (Section 4.3). In the following, feed-forward backpropagation NNs (http://gfesun1.gkss.de/software/ffbp) are used as a multiple nonlinear regression technique to parameterize the relationship between the radar intensity and ocean surface wind.

A NN is built up of several layers: an input layer, one or more hidden layers and one output layer. Each layer consists of 'neurons'; the input layer has as many neurons as input parameters, and the output layer as many neurons as output parameters. The number of hidden layers and number of neurons in the hidden layer(s) is dependent upon the problem. Each neuron in a layer is linked to each neuron of the neighboring layer with a weight.

An example of a NN with two hidden layers is given in Fig. 4.8. The output

value N_{out} of each neuron is derived according to

$$N_{\text{out}} = S\left(-N_{\text{bias}} + \sum_{i=1}^{n} w_i \, x_i\right), \qquad (4.2)$$

where N_{bias} is a bias value specific to each neuron, n is the number of incoming links, w is a weight specific to each neuron, x is the output value of the neuron in the preceding layer, and S is a non-linear function assuming monotonically increasing values between zero and one as the value of the argument goes from $-\infty$ to ∞. The most common choice, also used in the NNs applied here, is the sigmoid function $[1 + \exp(-x)]^{-1}$. A NN operates sequentially from layer to layer; output neurons of the first layer are given by the input values. The output of each neuron of the first hidden layer is computed by the summation of the weighted inputs, shifting by the bias and application of the nonlinear function. This is repeated for each layer until the output layer is reached, giving the results of the NN. To determine a NN, a sufficiently large set of input and output vectors has to be available to generate a training and a test sample. During the training of the NN, the values of the biases and weights are changed to minimize the error function. The resulting trained NN has to be tested with the test sample for its generalization power, e.g., whether reasonable results are produced for input values, which are not included in the training sample.

To take into account the dependencies of the RCS on Wind direction and range distance the mean RCS image (integrated over time) was subdivided in several range and azimuth bins. The range was subdivided into four 300 m intervals starting at 900 m and the azimuth into 5° bins. For each bin the mean RCS was retrieved.

The four range partitions were implemented to extend the sensitivity of the sensor on wind speed. The utilized radar system is only equipped with an 8-bit analogue
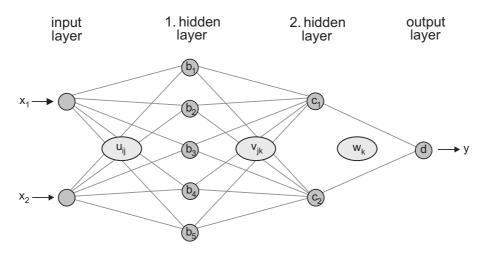

Figure 4.8: Schematic of a Neural Network (NN) having 2 input parameters, two hidden layers with 5 and 2 neurons, and an output layer with one parameter.
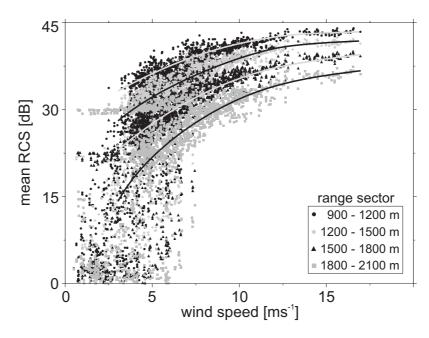
Figure 4.9: In situ measured wind speed is plotted versus mean RCS of the range sectors for each of the 3271 analyzed data sets. The curves were fitted to each of the range sectors.

to digital convertor and therefore saturation can occur for higher wind speeds especially in near range. In Fig. 4.9 the in situ measured wind speed is plotted versus the mean RCS of the range bins for each of the 3271 data sets. The superimposed curves were fitted to the points of each range bin. As expected the RCS decreases with range. However, more important for the wind speed retrieval, is the change of sensitivity on wind speeds with range. In the near range (900–1200 m) the sensitivity RCS on wind speed is higher at low wind speeds, while in the far range (1800–2100 m) the sensitivity is larger for high wind speeds. For this reason the utilization of the mean RCS from the different range sectors enables a significantly better parameterization for the entire range of wind speeds.

For the training of NNs all areas affected by shadows due to the platform equipment, the backscatter from neighboring platforms and the near range of up to 720 m from the radar antenna were neglected. The ratio between the training and test data set was set to 2:1.

In a first step NNs were trained using the RCS of each of the 4 range bins and the mean radar retrieved wind direction in respect to the antenna look direction as input and the in situ measured anemometer wind speed converted to 10 m height as output. Several different NNs were trained using all range-azimuth bins, range-azimuth bins within ± 15° upwind and/or down wind direction as well as range-azimuth bins within ± 15° of cross wind directions. The best result was found for the NN trained with the wind directions within ± 15° of both cross wind directions. This is due to the highest wind sensitivity at cross wind and due to artifacts caused by the neighboring platforms such as wind shadowing in the
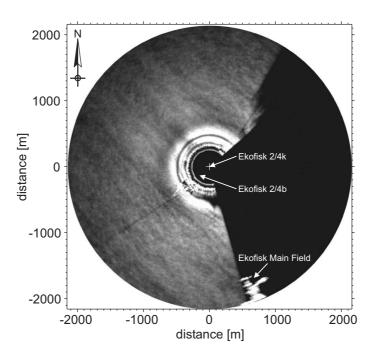
Figure 4.10: Wind shadowing due to the Ekofisk main field and Ekofisk 2/4 b,k.

downwind case and blockage in the upwind case.

In a second step NNs were trained with the RCSs of the 4 range bins in cross wind direction, the wind direction versus North and the radar look direction versus North as input and the wind speed at 10 m height as output. The resulting NN is composed of 3 hidden layers with 6 neurons in the first, 5 in the second and 4 in the third hidden layer. Comparison to the prior NN show a significant improvement concerning the main statistical parameters shown in Table 4.1.

input data set	corr.	bias	σ_{xy}
RCS, $\Delta\Phi_{(radar,wind)}$	0.95	0.03	1.11
RCS, Φ_{radar}, Φ_{wind}	0.96	0.01	0.97
RCS, $\Delta\vartheta_{(air,sea)}$, $\Delta\Phi_{(radar,wind)}$	0.96	0.03	0.95
RCS, $\Delta\vartheta_{(air,sea)}$, Φ_{radar}, Φ_{wind}	0.97	0.03	0.85

Table 4.1: Main statistical parameters resulting from the NNs considering the different input data.

This improvement is due to the dependence of the RCS on the radar look direction versus North, which are caused by side effects due to objects around the platform such as wind shadowing due to the large platform array South of Ekofisk 2/4 k. For example in Fig. 4.10 the wind blows from 141° with 14.5 ms^{-1}. It can be seen that in the Lee of the platform the backscatter of the ocean surface is significantly reduced in comparison to its surrounding, which is the wind shadowing effect of
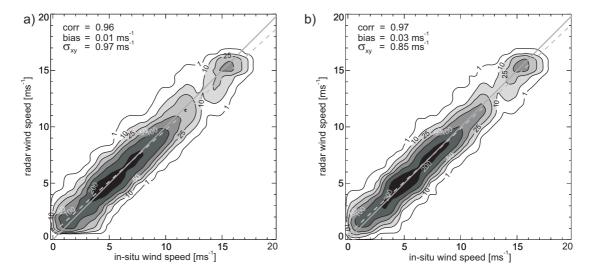
Figure 4.11: Scatterplots giving the comparison of the wind anemometer wind speeds (mean of 10 minutes) versus wind speeds retrieved from co-located nautical radar images. The radar wind speeds were retrieved in both cases using a NN with the intensity of the mean radar image and the wind direction from the co-located anemometer data as input. In (b) additionally the air-sea temperature difference has been considered for NN training.

the platforms (arrows in Fig. 4.10).

It is well know that the stratification conditions in the lower marine atmospheric boundary layer (MABL), mainly denoted by the air-sea temperature difference, affect the stability of the air-sea interface and therefore also the wind profile. In turn the wind profile influences the radar backscatter of the ocean surface. This leads at equivalent wind speeds in 10 m height to a higher radar backscatter of the ocean surface in case of an unstable MABL than for neutral and stable conditions [*Keller et al., 1989*]. For this reason in a third step a NN was trained considering, in addition to the NN trained in the second step, the air-sea temperature differences. The resulting NN consist of 3 hidden layers with 6 neurons in the first, 5 neurons in the second and 4 neurons in the third hidden layer. Again the main statistical parameters improve compared to the previously trained NNs, resulting in a correlation of 0.97, a negligible bias and a standard deviation of 0.85 ms^{-1} (see Table 4.1).

In Fig. 4.11 in-situ wind speeds are plotted against the wind speed resulting from nautical radar images using the last two NNs. The corresponding statistics of the comparison are given in the upper left of the scatter plots. Fig. 4.11a) gives the result of the second NN, which did not find a dependency on wind speeds below ≈ 2 ms^{-1}. In Fig. 4.11b the results of the third NN (including air-sea temperature differences) is shown, which enables the retrieval of wind speeds as low as ≈ 0.75 ms^{-1}.

In Fig. 4.12, the bias (black) and the standard deviation (grey) in wind speed of the comparisons of anemometer wind speeds to radar wind speeds are plotted for
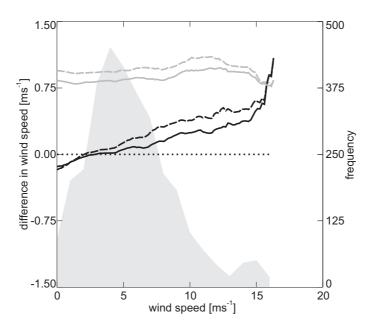
Figure 4.12: Bias (black curve) and standard deviation (grey curve) in wind speed of comparisons of anemometer wind speeds to radar wind speeds for intervals of 0.2 ms^{-1} for Fig. 4.11a (dashed) and Fig. 4.11b (solid). In addition the histogram of wind speeds is plotted.

intervals of 0.2 ms^{-1} for the NNs considered in Fig. 4.11a (dashed) and Fig. 4.11b (solid). In addition, a histogram of wind speeds is plotted. For wind speeds below 8 ms^{-1} the bias is very low and the standard deviation is rather constant. Above 8 ms^{-1} the bias increases significantly, which is due to the insufficient number of available data at higher wind speeds for the training of NNs. Comparing both NNs improves both statistical parameters when considering air-sea temperature differences.

To show the importance of the stratification conditions, the bias and standard deviation of the difference between radar and in-situ wind speed are plotted against the air-sea temperature difference (Fig. 4.13). Additionally, the mean wind speed for each air-sea temperature difference bin (dotted) and a histogram (grey filled) of all training and test data is given. For very unstable air-sea interfaces there is a high bias for the NN without considering the air-sea temperature difference (dashed curve). The NN is overestimating the wind speed, because with an unstable MABL, the RCS is larger than for a stable one. In the transition region the agreement is very good. For weakly stable conditions the NN is underestimating the wind speed, which corresponds to a decreasing RCS with increasing $\Delta\vartheta$. This is in agreement with theory and the observations of [*Keller et al., 1989*]. For very stable conditions the radar wind speeds are higher. This is explained with the nature of the NN, which has no information about the stratification conditions. Therefore it is averaging the low speed occurrences that also happened under unstable conditions with those under stable conditions. The result is an overestimation of radar wind speeds. Therefore the knowledge of the stratifica-
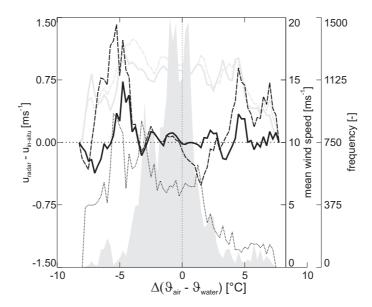
Figure 4.13: Bias (black curve) and standard deviation (grey curve) of radar retrieved wind speeds (with/without considered air-sea temperature difference (solid/dashed curve)) and in-situ wind speeds over air-sea temperature difference. The dotted black curve gives the mean wind speed for each air-sea temperature difference bin. A histogram (grey filled) of all training/test data sets is plotted.

tion conditions together with radar measurements are important. Considering the air-sea temperature difference results in an improvement of the bias for both the unstable and the stable conditions. The standard deviation is similar for both NNs.

4.6 Conclusions and outlook

The RCS of the ocean surface at X-band with HH polarization at grazing incidence is strongly dependent on the surface wind speed, wind direction, range distance and air-sea temperature differences. This provides the opportunity to develop an algorithm for remote measurements of the surface wind vectors from radar images. The resulting algorithm consists of two steps; one for wind direction and another for wind speed retrieval.

Wind directions are retrieved from wind induced streaks, which are oriented in wind direction and have a typical spacing of 100 to 500 m. The streak orientations are deduced by retrieving the local gradients of the mean RCS image, which results from integration of the radar image sequence over time as well as iterative smoothing and sub-sampling of the image. The resulting wind direction has a 180° ambiguity, which is removed by extracting the movement of wind gust patterns visible in the radar image sequence. Comparison to in situ measurements acquired at the radar platform and converted to 10 m height gave a correlation of 0.99 with

a bias of 0.6° and a standard deviation of 14.2°. It was also found that the wind direction retrieval accuracy increases with wind speed.

Wind speeds are retrieved from the dependence of the RCS on wind speed and wind direction. To parameterize the dependency of the RCS on the wind, NNs were trained considering different input parameters. Due to the missing radiometric calibration of the radar, the NNs have to be trained for each setup. The minimal parameters needed as input to the NN are the mean RCSs in cross wind direction at 4 different ranges, together with the radar retrieved wind direction in respect to the antenna look direction. It was found that cross wind is the best choice because the wind field is not disturbed by the platform itself. To take into account the dependence of the RCS on the stability in the lower MABL, the air-sea temperature difference has to be taken as additional input to the NN, showing a significant improvement of the wind speed retrieval. The latter is the best choice for radar setups aboard ships or platforms which are standing alone well off the coast. If the radar platform is situated at the coast or in the neighborhood of a larger object, e.g. another platform, the input of wind direction to the NN has to be differentiated. This allows the influence of the platforms neighborhood on the wind field to be taken into account, e.g. wind shadowing due to another platform. In the case of the data available from the Platform Ekofisk 2/4 k, the best results were obtained with input of the mean RCSs in cross wind direction at 4 different ranges, air-sea temperature differences and the radar retrieved differentiated wind direction. In comparison to in situ wind speeds measured at the platform and converted to 10 m height, the correlation is 0.97 with a bias of 0.03 ms^{-1} and a standard deviation of 0.85 ms^{-1}.

It is not always possible to setup up temperature sensors to measure the air-sea temperature difference, e.g. on ship-borne installations. Comparing the plots in Fig. 4.11 shows that the parametrization without implemented air-sea temperature information already gives very good and practicable results. The radar system can therefore be installed without any other additional sensors for wind measurements. In contrast to typical in-situ sensors like anemometers, the measurements of the radar system are not influenced by movements of ships or platforms and local turbulences due to installations.

The method is extended to retrieve high resolution wind fields from the radar image sequences. The wind directions are retrieved from the wind induce streaks via local gradients with a resolution of 120 m. For the wind speeds, a NN was trained considering the mean RCS, distance to antenna as well as wind direction and antenna look direction versus North. Fig. 4.14 shows the resulting wind field with a resolution of 240 m in case of the whole radar image as well as 120 m concerning the cutout.

In future more data sets from Ekofisk 2/4 k will be considered for the purpose of investigating a larger bandwidth of wind speeds for improving of the results
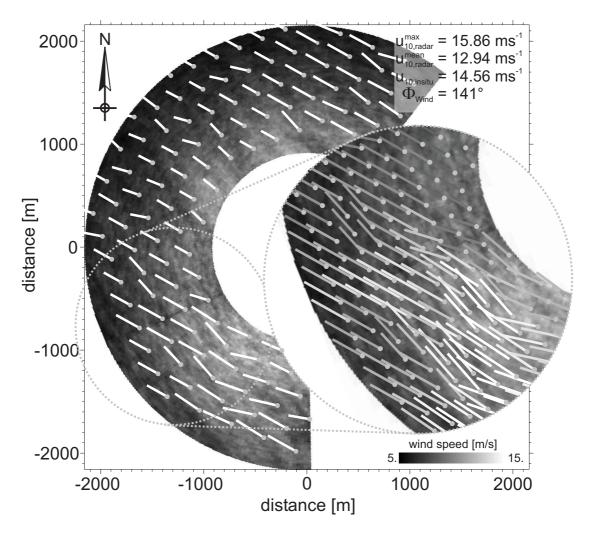
Figure 4.14: High-resolution ocean wind field retrieved at Ekofisk 2/4k on March, 27th 2001 using the determined local wind directions together with an NN that parameterizes the wind speed spatially.

and finding the limitations of the radar system. *Hatten et al. Hatten et al., 2003* could show that for $23\ ms^{-1}$ no saturation occurs. Furthermore, the wind induced streaks are used to retrieve wind vectors locally, spatially and temporally [*Dankert et al., 2003b*].

Acknowledgments

Bibliography

Alpers, W. R., Ross, D. B., and Rufenach, C. L. (1981). On the detectability of ocean surface waves by real and synthetic aperture radar. *J. Geophys. Res.*, 86, 6 481–6 498.

Bell, P. (1999). Shallow water bathymetry derived from an analysis of x-band marine radar images of waves. *Coastal Eng.*, 37, 513–527.

Borge, J. N., Hessner, K., and Reichert, K. (1999). Estimation of the significant wave height with x-band nautical radars. In *Proc. 18th Intern. Conf. on Offshore Mech. and Arctic Eng. (OMAE)*, number OMAE99/OSU-3063 St. John's, Newfoundland, Canada.

Borge, J. N., Rodríguez, G., Hessner, K., and González, P. (in press 2003). Inversion of nautical radar images for surface wave analysis. *J. Atmos. and Ocean Tech.*

Brown, G. (1998). *Special issue on low-grazing angle backscatter from rough surfaces*, volume 46 of *IEEE Trans. Antennas Propag.* IEEE.

Chaudhry, A. and Moore, R. (1984). Tower based backscatter measurements of the sea. *IEEE Journal of Oceanic Engineering*, 9, 309–316.

Dankert, H. (2003). Retrieval of surface-current fields and bathymetries using radar-image sequences. *Proc. Int. Geosci. Remote Sens. Symp.*

Dankert, H., Horstmann, J., Lehner, S., and Rosenthal, W. (2003a). Detection of wave groups in SAR images and radar-image sequences. *IEEE Trans. Geosci. Remote Sens.*, 41(6), 1 437–1 446.

Dankert, H., Horstmann, J., Magnusson, A., and Rosenthal, W. (2003b). Ocean winds retrieved from x-band radar-image sequences. *Proc. Int. Geosci. Remote Sens. Symp.*

Fetterer, F., Gineris, D., and Wackerman, C. (1998). Validating a scatterometer wind algorithm for ERS-1 SAR. *IEEE Trans. Geosci. Remote Sens.*, 36(2), 476–492.

Gerling, T. (1986). Structure of the surface wind field from Seasat SAR. *J. Geophys. Res.*, 91, 2 308–2 320.

Hatten, H., Seemann, J., Horstmann, J., Senet, C., and Ziemer, F. (submitted 2003). Azimuthal and range dependency of sea-surface radar backscatter at hh-polarization and low grazing incidence. *IEEE Trans. Geosci. Remote Sens.*

Horstmann, J., Koch, W., Lehner, S., and Tonboe, R. (2002). Ocean winds from RADARSAT-1 ScanSAR. *Can. J. Remote Sens.*, 28(3), 524–533.

Horstmann, J., Schiller, H., Schulz-Stellenfleth, J., and Lehner, S. (2003). Global wind speed retrieval from SAR. *IEEE Trans. Geosci. Remote Sens.*, 41(10).

Jähne, B., Haußecker, H., and Geißler, P. (1999). *Handbook of Computer Vision and Applications*. Academic Press.

Keller, W., Wismann, V., and Alpers, W. (1989). Tower-based measurements of the ocean C band radar backscattering cross section. *J. Geophys. Res.*, 94, 924–930.

Keller, W. C., Plant, W. J., Petitt, R. A., and Terray, E. A. (1994). Microwave backscatter from the sea: Modulation of received power and Doppler bandwith by long waves. *J. Geophys. Res.*, 99, 9 751–9 766.

Keller, W. C., Plant, W. J., and Weissman, D. (1985). The dependence of X band microwave sea return on atmospheric stability and sea state. *J. Geophys. Res.*, 90, 1 019–1 029.

Koch, W. (in press, 2003). Directional analysis of SAR images aiming at wind direction. *IEEE Trans. Geosci. Remote Sens.*

Lee, P., Barter, J., Beach, K., Hindman, C., Lake, B., Rungaldier, H., Shelton, J., Williams, A., Lee, R., and Yuen, H. (1995). X-band microwave backscattering from ocean waves. *J. Geophys. Res.*, 100, 2 591–2 611.

Lee, P., Barter, J., Caponi, E., Caponi, M., Hindman, C., Lake, B., and Rungaldier, H. (1996). Wind-speed dependence of small-grazing-angle microwave backscatter from sea surfaces. *IEEE Trans. Antennas and Propagation*, 44(3), 333–340.

Lehner, S., Horstmann, J., Koch, W., and Rosenthal, W. (1998). Mesoscale wind measurements using recalibrated ERS SAR images. *J. Geophys. Res.*, 103, 7 847–7 856.

Richaume, P., Badran, F., Crepon, M., Mejia, C., Roquet, H., and Thiria, S. (2000). Neural network wind retrieval from ERS-1 scatterometer data. *J. Geophys. Res.*, 105, 8 737–8 751.

Schiller, H. and Doerffer, R. (1999). Neural network for emulation of an inverse model — Operational derivation of case II water properties from MERIS data. *Int. J. Remote Sens.*, 20(9), 1 735–1 746.

Senet, C., Seemann, J., and Ziemer, F. (2001). The near-surface current velocity determined from image sequences of the sea surface. *IEEE Trans. Geosci. Remote Sens.*, 39, 492–505.

Trizna, D. (1997). A model for brewster angle effects on sea surface illumination for sea scatter studies. *IEEE Trans. Geosci. Remote Sens.*, 35(5), 1232–1244.

Trizna, D. (2001). Errors in bathymetric retrievals using linear dispersion in 3-d fft analysis of marine radar ocean wave imagery. *IEEE Transactions on Geoscience and Remote Sensing*, 39, 2465–2469.

Trizna, D. and Carlson, D. (1996). Studies of dual polarized low grazing angle radar sea scatter in nearshore regions. *IEEE Trans. Geosc. Remote Sens.*, 34, 747–757.

Vachon, P. W. and Dobson, F. (1996). Validation of wind vector retrieval from ERS-1 SAR images over the ocean. *Global Atmos. Ocean Syst.*, 5, 177–187.

Wackerman, C., Horstmann, J., and Koch, W. (2003). Operational estimation of coastal wind vectors from RADARSAT SAR imagery. *Proc. Int. Geosci. Remote Sens. Symp.*, (pp. this issue).

Wetzel, L. (1990). Electromagnetic scattering from the sea at low grazing angles. *Surface Waves and Fluxes, Geernaert and W.J. Plant (eds.), Kluwer Academic Publishers*, II, 109–171.

Wetzel, L. (1995). *Radar Handbook*, chapter Sea Clutter. Addison Wesley Publishing Company.

Chapter 5

Ocean Surface Determination from X-band Radar-Image Sequences

Heiko Dankert and Wolfgang Rosenthal

GKSS Research Center, 21502 Geesthacht, Germany

Abstract

An empirical inversion method for determination of time series of ocean surface elevation maps from nautical radar-image sequences is presented. The method is based on the determination of the tilt angle at each pixel in the radar images. Thereby in-situ sensors are not required. A calibration is not necessary. A conventional nautical radar is used as a sensor. Radar-image sequences, with their high spatial resolution and large coverage, offer a unique opportunity to derive and study individual waves and wave fields in space and time and therefore allow the measurement of individual wave parameters and wave groups. For validation of the inversion scheme, the significant wave heights derived from the inverted radar data sets and from co-located wave records are compared. It is shown that the accuracy of the radar-retrieved significant wave height is within the accuracy of the in-situ sensors. Furthermore, a wave elevation time series is directly compared to a buoy record to show the capabilities of the proposed method.

5.1 Introduction

Ocean waves are imaged by a nautical radar because the long surface gravity wave modulate the radar backscatter from the sea surface. Thereby the small scale roughness of the sea surface raises the backscatter of the electromagnetic waves. This phenomenon is called sea clutter [*Wetzel, 1990*]. The modulation due to the long surface waves is a sum of the four contributing processes: tilt, hydrodynamic, and wind modulation, and the geometrical effect of shadowing.

The ocean surface elevation is typically measured with one-dimensional (1-D) in-situ sensors such as buoys, laser sensors, or wave gauges with high accuracy. These sensors are placed on certain and carefully chosen positions in measurement areas, off-shore close to platforms, near shore areas or in harbors. Off-shore, the sea state conditions are typically homogeneous, the statistical properties of the sea surface are not changing from one location to the next in the measurement area. Close to the coast, inside harbors or behind off- and near-shore buildings and structures, the sea state becomes inhomogeneous. The sea state parameters, which have been measured by the 1-D in-situ sensors, are not transmissible to neighbored locations. Further, there is a lack of directional information about the wave fields. The sea state is therefore incompletely captured by such sensors. The possible positions of such sensors is limited on the mooring requirements, e.g. for a wave rider buoy the given water depth and the maximum current speed are important.

The limitation of observing the sea surface at a fixed location over time is overcome by measuring with an imaging sensor such as a nautical radar. The radar scans temporal sequences of consecutive radar images of the ocean surface $\eta(\vec{r}, t)$ at grazing incidence from towers and ships. It operates at X-band and has the capability to measure the backscatter from the ocean surface in space $\vec{r} = (x, y)$ and time t under most weather conditions, independent of light conditions.

In addition to the ocean surface retrieval presented here, nautical radar image sequences of the sea surface are also used to determine other hydrographic parameters. In particular they have been used to determine: two-dimensional wave-spectra and significant wave heights [*Borge et al., 1999*], individual wave parameters [*Borge et al., 2003*], wave groups [*Dankert et al., 2003a*], the near surface current [*Senet et al., 2001*], and bathymetry [*Bell, 1999, Trizna, 2001*]. Recently, new methods for the current and bathymetry field retrieval from nautical radar image sequences have been developed [*Dankert, 2003*]. Nautical radar image sequences are further used for the retrieval of high-resolution ocean wind fields [*Dankert et al., 2003b*].

The investigations presented in this study were performed with data sets collected by a radar system installed aboard a platform in the Norwegian oil field Ekofisk in the central North sea using the Wave Monitoring System (WaMoS). This system uses a conventional nautical radar as sensor. Accordingly, all measurements were

taken with horizontal (HH) polarization at grazing incidence.

The square root of the signal-to-noise ratio (SNR) of nautical radar-image sequences is proportional to the significant wave height of the observed wave field [*Ziemer, 1995*]. This is in accordance to the synthetic aperture radar (SAR), where the SNR is also used for the calibration of the image spectra [*Alpers and Hasselmann, 1982, Plant, 1991*]. The calibration of image spectra using the SNR is based on the assumption that the radar backscatter in the analyzed area is a Gaussian distribution [*Alpers and Hasselmann, 1982*]. During the calibration phase for the radar-image sequence image spectra the calibration constants have to be determined by taking co-located in-situ measurements, e.g. from buoy or laser measurements. After this calibration phase the system works as stand-alone instrument. Based on this technique *Borge et al., 2003* has introduced an inverse modelling technique for retrieving the ocean surface elevation. The method is based on the determination of the modulation transfer function (MTF) between the radar image spectrum and a in-situ sensor heave spectrum. To obtain the MTF a calibration phase needs to be carried out. The estimated MTF is applied to the amplitudes of the complex radar image spectrum and only to those components that contain spectral energy of the linear surface gravity waves. The phases of these components are also retained.

This paper introduces an empirical method for the determination of the ocean surface elevation in space and time for the radar-image sequences. Thereby no calibration is necessary. No in-situ measurements are required. The method is based on the determination of the tilt angle at each pixel of the radar images.

For validation of the method co-located measurements from three in-situ sensors, one wave rider buoy and two laser sensors, were taken. The validation phase is divided into two steps. In the first step, a comparison of the significant wave height as statistical integral spectral parameter from the inverted radar-image sequences and the co-located in-situ data is performed. The second phase is a deterministic comparison. Subsequently a wave profile measured by the buoy is compared to the co-located radar-derived ocean surface time series at the location of the buoy. The wave rider buoy is thereby directly seen by the radar. The laser sensors are also located in the measurement area of the radar, but in a shadowed region, and therefore unsuitable for this direct comparison.

The paper is organized as follows: In Section 5.2 the radar system and available data are introduced. Section 5.3 gives a theoretical introduction into the radar imaging processes. In Section 5.4 the ocean surface retrieval algorithm is introduced and applied to radar data sets. The radar retrieved significant wave heights are compared to the co-located in-situ values in section 5.5. Further, a deterministic comparison is performed and the retrieved spectra are considered. Finally, in Section 5.6, conclusions and an outlook are given.

5.2   Investigated data

The measurements have been carried out from the platform "2/4k" of the Ekofisk oil field operated by ConocoPhillips in the North Sea at 56.5° North and 3.2° East. The water depth in this area is about 70 m. The radar measurements are performed operationally by a typical nautical radar together with a WaMoS II unit, which allows for the continuous digitization of time series of polar nautical radar images. They are used for the determination of 2-D wave spectra and integral sea state parameters like peak wave length, peak period, and the estimation of the significant wave height in comparison to a common wave rider buoy and two laser sensors in this area. The near surface current velocity is estimated. The radar data are compared to co-located synthetic aperture radar (SAR) measurements. Furthermore, the radar-image sequences are used for the determination of high-resolution wind vector fields [*Dankert et al., 2003b*].

In Fig. 5.1 the platform, the location of the installed radar system, the in-situ sensors, and a recorded sample radar-image sequence are shown. The nautical radar was operated at 9.5 GHz (X-band) with horizontal (HH) polarization in transmit and receive at grazing incidence. The radar antenna is installed at the North-West corner of the platform marked by the black arrow. The installation height of the antenna is 74 m above the mean sea level. The radar system is operationally recording data sets of 32 images. The time interval between 2 consecutive images is $\Delta t = 2.56$ s. A complete time series therefore covers a time period of $T_{tot} \approx 82$ s. The radar covers an area within a radius of about 2 km. The polar images are converted to rectangular coordinates. The grid size is chosen to be equal to the radar resolution of $\Delta r \approx 10$ m. The radar-image sequence shows a wave field, which is propagating in a Northern direction. The dark patches in the radar images are due to the platform equipment, e.g. the helicopter deck and the lattice towers. The higher backscatter in the south originates from the other platforms of the oilfield, which are also visible in the foreground of the photo. For the investigations, only areas representing backscatter from the sea surface are considered. The range-ring patterns in the near range are caused by multiple reflections of the antenna side lobes in the near-field from the host platform equipment in a distance of about 500m, due to the longer running time of the radiated energy. To negate this effect the data are corrected by the antenna pattern.

The analogue output of the radar systems video signal is sampled by a Digital Scan Converter (DSC) with a sampling frequency of $f_{AD} = 20$ Mhz. The sampling frequency gives a radial resolution of $\Delta r = c/(2f_{AD}) = 7.5$ m, where c denotes the speed of light. In the near range of the antenna (0 m - 240 m) the radar signal has not reached the water surface due to the limited vertical directivity and the installation height. There is no backscatter in this so-called dead range area. Therefore the DSC is delayed so as to detect only the radar backscatter from the end of the dead range. This area is visible in the radar image in Fig. 5.1. With
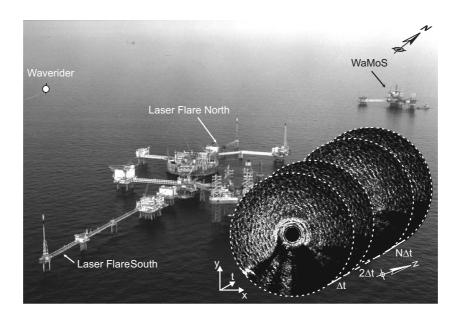
Figure 5.1: Ekofisk 2/4 k platform of the Ekofisk oil field in the North Sea. The WaMoS system is installed at the North-West corner on the platform in the background. In the radar images several shadows are visible, which are due to the equipment of the platform. The large backscatter in the south originates from the oil field visible in the foreground of the photo. A wave rider buoy is placed near the oil field and within the radar measuring range. The two laser sensors are mounted on the main complex.

256 samples in range, the covered area by the antenna is from 240 m to ≈ 2160 m.

Nautical radar systems are equipped with a logarithmic amplifier and are not radiometrically calibrated. Therefore, the normalized RCS could not be determined. The backscattered signal of each radar resolution cell is digitized with 8 bit, which allows grey values between 0 (no backscatter) and 255 (highest signal).

Radar data sets with co-located in-situ data were available for the investigations during 2001. The significant wave height during that period was up to $H_S \approx 7$ m. The wind speed range was between $0\ ms^{-1}$ and $\approx 17\ ms^{-1}$.

The in-situ data, provided by one wave-rider buoy and two laser sensors (see Fig. 5.1), are continuous measurements of the sea surface elevation, whereas the sea state parameters are determined for time intervals of 20 minutes. The sampling frequency is 2 Hz.

Information about the precipitation has not been recorded. The reduction of the radar backscatter from the sea surface due to oil spills can be neglected.

5.3 Modulation mechanisms

The sea state is imaged by a radar, because the radar cross section (RCS) of the ocean surface is modulated by the long surface gravity waves, which are within the resolution of the radar. This modulation of the RCS is mathematically described by the modulation transfer function (MTF), which is defined as expansion of the RCS for the spectral amplitudes of the wave field $\hat{\eta}(\vec{k})$ [*Alpers et al., 1981*]:

$$\sigma_0 = \overline{\sigma}_0 + \delta\sigma_0 = \overline{\sigma}_0 \cdot \left(1 + \int M(\vec{k}) \cdot e^{i(\vec{k}\cdot\vec{r} - \omega(\vec{k})\cdot t)} d\hat{\eta}(k)\right), \qquad (5.1)$$

with the mean RCS $\overline{\sigma}_0$, the modulation part $\delta\sigma_0$, the wave number vector $\vec{k}$ and the angular frequency $\omega(\vec{k})$. The MTF is hermitian as well as the spectral amplitudes because of the real-valued RCS $(M(-\vec{k}) = M^*(\vec{k}))$, and therefore also includes the phase information of the imaged ocean waves. The MTF is a sum of the contributing processes: the geometrical effects of shadowing and tilt, hydrodynamic modulation, and wind modulation:

$$M = M_{shad} + M_{tilt} + M_{hydr} + M_{aero}. \qquad (5.2)$$

Under grazing incidence parts of the imaged sea surface cannot be seen by the radar; they are shadowed by the waves. Shadowing appears, if the shadowing parameter, defined to be the ratio between the root mean square tilt of the sea surface and the depression angle $\Psi = 90° - \Theta$, has values $\eta_s \geq 1$ [*Bass and Fuks, 1979*]. Thereby the wave amplitudes have to be high enough. In the case of Ekofisk, with an antenna height of 74 m, this modulation mechanism appears only in the very far range. Θ denotes the incidence angle, describing the angle between the perpendicular of the ocean surface and the radar beam.

Tilt modulation is a purely geometric effect which leads to a higher radar backscatter from a wavefront which is directed towards the radar. The long ocean waves tilt the facets from the horizontal plane towards and away from the radar. This leads to a change of local incidence angles and therefore to a change of radar backscatter, which increases with decreasing incidence angle. The expansion of the RCS for the local tilt components is given by *Alpers et al., 1981*:

$$\begin{aligned}
\left(\frac{\delta\sigma_0}{\overline{\sigma}_0}\right) &= \frac{1}{\overline{\sigma}_0} \cdot \left.\frac{\partial\sigma_0}{\partial\vec{n}}\right|_{\vec{n}=(0,0,1)} \cdot \vec{n} && (5.3) \\
&= \frac{1}{\overline{\sigma}_0} \cdot \left.\frac{\partial\sigma_0(\Theta, \varphi, \delta=0)}{\partial\tan\varphi}\right|_{\varphi=0} \frac{\partial\eta}{\partial x} \\
&\quad + \frac{1}{\overline{\sigma}_0} \cdot \left.\frac{\partial\sigma_0(\Theta, \varphi=0, \delta)}{\partial\tan\delta}\right|_{\delta=0} \frac{\partial\eta}{\partial y},
\end{aligned}$$

whereas $\vec{n}$ is the vector perpendicular to the ocean surface, $\tan\varphi = \partial\eta/\partial x$ gives the tilt component of the surface in the plane of incidence, $\tan\delta = \partial\eta/\partial y$ the tilt

component perpendicular to this plane. With the Fourier expansion of the wave field the transfer function, tilt modulation respectively, to the first order is given by *Alpers et al., 1981*

$$M_{\text{tilt}} = M_{\text{p}} + M_{\text{n}}, \tag{5.4}$$

with

$$M_{\text{p}} = \frac{1}{\sigma_0} \left. \frac{\partial \overline{\sigma}}{\partial \tan \varphi} \right|_{\varphi=0} \iota \vec{k}_{\text{p}},$$

and

$$M_{\text{n}} = \frac{1}{\sigma_0} \left. \frac{\partial \overline{\sigma}}{\partial \tan \delta} \right|_{\delta=0} \iota \vec{k}_{\text{n}},$$

where M_{p} and M_{n} are the M_{tilt} components parallel and normal to the look direction of the radar, ι describes the phase shift of 90° of the ocean waves in the image, and $\hat{k}_{\text{p}}$ and $\hat{k}_{\text{n}}$ are components of the wave number vector. The azimuth has a strong influence on the tilt modulation. Thereby the strongest modulation occurs if the antenna is viewing directly in wave travel direction or 180° to it, whereas parallel to the crests of single wave components there is no modulation contribution [*Moore, 1985*].

The hydrodynamic modulation describes the modulation of the amplitude and phase of the capillary waves by the interaction with the orbital velocity field of the long surface waves. This effect is indicated by convergence zones on the wave fronts and divergence zones on the wave back. The resulting modulation of spectral density of the Bragg waves is described by a two-scale modell [*Alpers and Hasselmann, 1978*] and an improved three-scale modell [*Romeiser et al., 1994*]. Under grazing incidence at HH polarization, the discrete scattering elements are mainly contributing to the RCS of the ocean surface. These elements are increased by the hydrodynamic modulation [*Shyu and Phillips, 1990*]. The hydrodynamic modulation is neglected in the method developed here.

The wind modulation is based on the variation of the wind-induced friction velocity along the ocean surface. Estimates of the modulation of the friction velocity have been carried out by [*Hara and Plant, 1994*]. They found that the influence of wind modulation on Bragg waves is stronger than on the longer ocean waves. Further investigations on wind modulation have been performed by [*Wright and Keller, 1980, Smith, 1990, Romeiser et al., 1997, Romeiser and Alpers, 1997*].

The spectral description of the RCS regarding (5.1) is applicable for low to moderate sea states [*Alpers et al., 1981*]. For higher sea states *Wright, 1968* suggested to subdivide the ocean surface into local facets, which are relatively small to the long ocean surface waves, but within the radar resolution. Here, the developed empirical method is based on this spatial description. For a local facet at location

$\vec{r}$ and time t the local RCS is given by:

$$\sigma_0(\vec{r},t) = \overline{\sigma}_0(\vec{r},t) + \delta\sigma_0(\vec{r},t) = \overline{\sigma}_0(\vec{r},t) \cdot \left(1 + M(\vec{\vec{k}}|\vec{r},t) \cdot \underbrace{e^{i\vec{\vec{k}}\cdot\vec{r}} \cdot A(\vec{r},t)}_{\eta(\vec{r},t)} \right), \quad (5.5)$$

describing the variation of the RCS $\delta\sigma_0$ at location $\vec{r}$ and time t as a product of the local modulation function $M(\vec{\vec{k}}|\vec{r},t)$ and the local wave field $\eta(\vec{r},t)$ as indicated in (5.5). Thereby the local wave field is a product of a carrier wave with wave number $\vec{\vec{k}}$ and a slowly varying amplitude function $A(\vec{r},t)$. The local transfer function for the facet and the carrier waves amplitude and therewith the RCS is described by the geometrical effects of shadowing and tilt of the long surface waves, as well as wind:

$$M = M_{shad} + M_{tilt} + M_{aero}. \quad (5.6)$$

The frictional force of the local wind is generating the small-scale roughness of the sea surface, which raises the RCS and therewith the variance of the mean RCS $\overline{\sigma}_0$.

In the introduced method the local RCS σ_0 in space and time of the ocean surface is given by

$$\sigma_0(\vec{r},t) := \begin{cases} \overline{\sigma}_0(\vec{r},t) \cdot \vec{a}(\vec{r},t) \cdot \vec{n}(\vec{r},t) & if\ \eta(\vec{r},t)\ illuminated \\ min(\sigma_0) & if\ \eta(\vec{r},t)\ shadowed \end{cases}, \quad (5.7)$$

which is in regard to (5.3), and where $\vec{n}(\vec{r},t)$ is the vector perpendicular to the ocean surface and $\vec{a}(\vec{r},t)$ gives the unit vector, which is pointing from the surface $\vec{\eta}(\vec{r},t)$ to the radar antenna. For this approach at grazing incidence the RCS is proportional to the local depression angle and independent from the azimuthal tilt of the ocean surface. Therefore, azimuthal travelling plane wave components are not imaged by the radar. The azimuthal dependency of the modulation of the RCS by the ocean waves are correctly described by the model. Regarding (5.7) the tilt modulation is assumed to be linearly related to the local incidence angle.

5.4 Method

This chapter is describes the steps of the empirical method for retrieving the ocean surface from radar-image sequences. The input for the method are the raw polar radar-image sequences $\sigma_0(\vec{r},t)$ acquired by the WaMoS system. The method is demonstrated with the radar-image sequence in Fig. 5.2, recorded on June 3rd, 2001 at Ekofisk 2/4k.
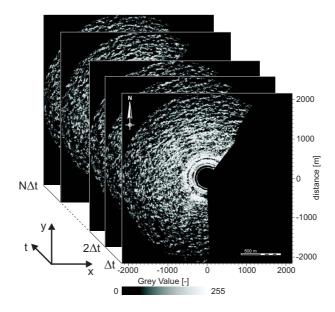
Figure 5.2: Radar-image sequence recorded on June 3rd, 2001 at Ekofisk 2/4k.

5.4.1 Radar pattern

Nautical radar antennas are directional antennas, which radiate radio-frequency energy in patterns of lobes or beams that extend outward from the radar antenna in one direction for a given antenna position. The radiation pattern also contains minor lobes, but these are weak and normally have little effect on the main radiation pattern. However, in the case of Ekofisk range-ring patterns appear in the near range (Fig. 5.1), caused by multiple reflections of these antenna side lobes in the near-field from the host platform equipment as mentioned already in chapter 5.2. The main lobe varies in angular width 0.9° and vertically 21°. Because of the radiation pattern, each radar antenna has a typical receiving pattern. An important step to analyze the radar images is to know this receiving pattern and to correct the data.

For measuring, the antenna receiving pattern radar images have to be measured in an area that provides a homogeneous RCS over the entire measurement area. For synthetic aperture radar images this is done by taking images from the rainforests. For the nautical radar system it is not possible to take measurements like this. By taking the total time average of the radar images of all given data sets from the Ekofisk installation, the radar-typical receiving pattern is determined with an additional constant RCS term due to wind modulation as shown in Fig. 5.3. By transforming the total mean RCS image into the spectral domain with a 2-D Fast Fourier Transform (FFT) the constant term is filtered out. After applying an inverse 2-D FFT the antenna pattern is determined. Fig. 5.4 shows the result, a 1-D radial cut through the 2-D antenna receiving pattern (Fig. 5.3), beginning at the image center.
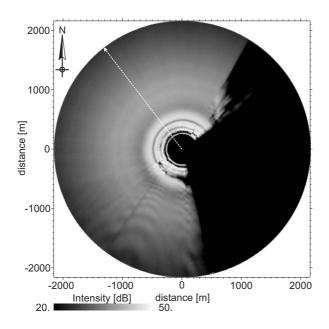
Figure 5.3: Determined antenna receiving pattern of the radar system mounted on the Ekofisk 2/4k platform. The image still contains an additional RCS term due to wind modulation. The dashed line indicates the cut shown in Fig. 5.4.
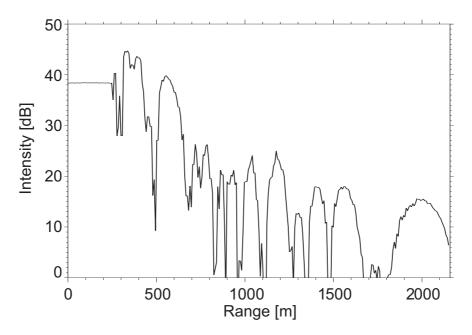

Figure 5.4: 1-D radial cut through the 2-D antenna receiving pattern of Fig. 5.3, beginning at the center of the image. The constant RCS term due to wind modulation has been removed. The dead range is from 0 m - 240 m and is not considered here.

All images of a given radar-image sequence $\sigma_0(\vec{r}, t)$ are corrected with the 2-D antenna pattern. Fig. 5.5 is exemplary showing a corrected radar image of the sequence of 32 images.
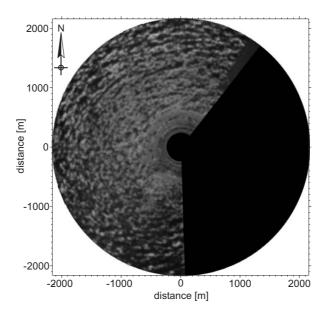
Figure 5.5: Image of 32 of a radar-image sequence, corrected by the radar receiving pattern. The data set was recorded on June 3rd, 2001 at Ekofisk 2/4k.

5.4.2 Parametrization of mean RCS

Regarding (5.3), the variation of the RCS $\delta\sigma_0$ from the mean RCS $\overline{\sigma}_0$ is assumed to be mainly caused by the tilt modulation and shadowing of the RCS due to the long ocean surface waves. The mean RCS is therefore parameterized. Because the radar is imaging the ocean surface beam by beam, and the radar is mainly imaging range-travelling waves, an effective way for the parametrization is 1-D for each radar beam. This is performed by fitting a 3rd-order polynomial curve through the mean RCS:

$$\tilde{\sigma}_{0,i}(r, \phi_i) = f(r, \phi_i), \tag{5.8}$$

where $\tilde{\sigma}_0$ gives the resulting 2-D parametrization function, build up beam by beam in azimuth (i denotes the beam number), by using a least-squares method. Fig. 5.6 shows exemplarily the parametrization of the mean RCS.

5.4.3 Determination of tilt angle

Additionally to the parametrization of the mean RCS, the local radar depression angle is required to retrieve the local tilt angle of the ocean surface. For a given installation height of the radar antenna $h_{ant} = 74$ m the range-depending depression angle, which is $\Psi = 90° - \Theta$ is given by:

$$\tilde{\Psi}(r, \phi) = \arctan(\frac{h_{ant}}{r}), \tag{5.9}$$
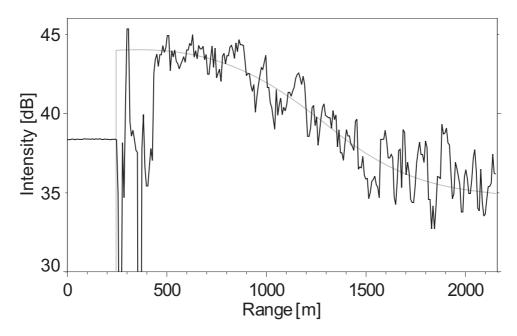
Figure 5.6: Parametrization $\tilde{\sigma}_{0,i}(r,\phi_i)$ (grey) of the mean RCS $\overline{\sigma}_0(r,\phi_i)$ of one radar beam for the first image of the radar-image sequence, corrected by the radar receiving pattern.
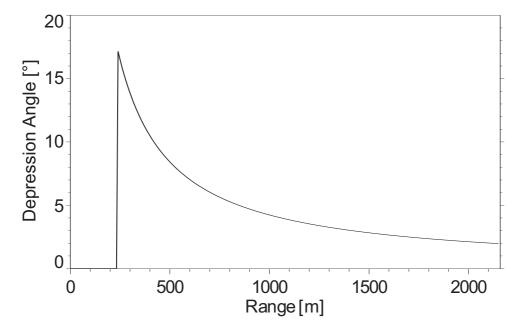

Figure 5.7: Range-dependent depression angle for a given antenna height of 74 m above the mean sea level at Ekofisk 2/4k.

with (r,ϕ) giving the location relative to the antenna in polar coordinates. The depression function is shown in Fig. 5.7.

The parametrization of the mean RCS $\tilde{\sigma}_0(r,\phi)$ gives the RCS of the ocean surface without sea state at each location in range and azimuth direction. The change
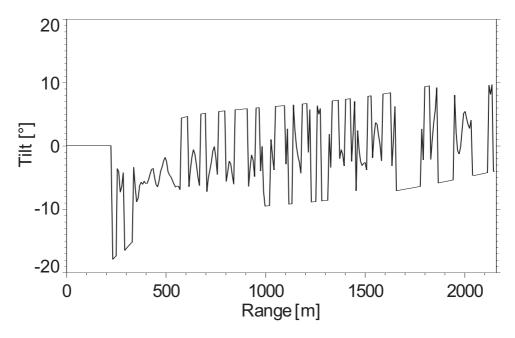
Figure 5.8: Range-dependent tilt angle for a given antenna height of 74 m above the mean sea level at Ekofisk 2/4k.

of the RCS $\delta\sigma_0$ due to modulation of $\overline{\sigma}_0$ is assumed to be directly related to the change of the tilt Ψ of the ocean surface. With the parameterizations for both, the mean RCS and the depression angle, a certain depression angle for a certain RCS value is given.

At a given location (r_0, ϕ_0) the tilt angle φ is retrieved by determining the difference of the depression angles:

$$\varphi(r_0, \phi_0) = \Psi_1(r_0, \phi_0) - \Psi_0(r_0, \phi_0), \tag{5.10}$$

where Ψ_1 is the depression angle at the location, where the parametrization $\tilde{\sigma}_0$ regarding (5.8) is equal to $\sigma_0 = \overline{\sigma}_0 + \delta\sigma_0$:

$$\Psi_1(r_0, \phi_0) = \tilde{\Psi}(r_1, \phi_0) = \tilde{\Psi}(f_{\tilde{\sigma}_0}^{-1}(\sigma_0, \phi_0), \phi_0). \tag{5.11}$$

Ψ_0 is the depression angle at (r_0, ϕ_0):

$$\Psi_0(r_0, \phi_0) = \tilde{\Psi}(r_0, \phi_0). \tag{5.12}$$

In Fig. 5.8 the resulting tilt angles for one radar beam are exemplarily shown. The tilt angles vary within the given range of the depression angles. For RCS values σ_0 exceeding the domain of $\tilde{\sigma}_0$ the limit values of $\tilde{\Psi}$ are assigned. The local tilt angles are determined for each radar image of a radar-image sequence. The result is a sequence of tilt images $\Phi(\vec{r}, t)$.

5.4.4   Determination of ocean surface elevation

The ocean surface elevation $\eta(\vec{r}, t)$ is determined from the tilt angles $\Phi(\vec{r}, t)$ directly by integration over the space coordinates $\vec{r}$. In the spatial domain the integration is performed by convoluting the tilt images with a 2-D integration filter kernel. A convolution in the spatial domain corresponds to a multiplication in the Fourier space. This is an effective way for the numerical integration. The transfer function of an ideal integration filter is purely imaginary and proportional to the wave number:

$$\hat{D} = ik^{-1}|\cos(\phi_W - \phi_A)|^{-1} \quad \forall\, k > 0, \tag{5.13}$$

where k gives the modulus of the wave number vector $\vec{k}$, Φ_W is the wave travel direction and ϕ_A the antenna look direction. The function is complex and shifts the phase of all wave number components in the Fourier space by $\pi/2$. The smaller the wave numbers are, the more they are amplified. The modulus of the wave numbers depends on the wave travel direction relative to the antenna look direction.

The tilt-image sequence $\Phi(\vec{r}, t)$ is transformed in the wave-number frequency domain with a 3-D FFT. The resulting 3-D tilt spectrum $\hat{\Phi}(\vec{k}, \omega)$ is integrated by multiplying with the integration transfer function $\hat{D}$:

$$\hat{\eta}(\vec{k}, \omega) = \hat{\Phi}(\vec{k}, \omega) \cdot \hat{D}. \tag{5.14}$$

The result is a complex 3-D wave spectrum of the ocean surface elevation field.

As mentioned previously, the division by the wave numbers causes an asymptotically increase of the amplitudes for very small wave numbers. A filtering process is therefore necessary to retrieve only the signal of the ocean surface wave field itself when transforming the 3-D wave spectrum into the spatial-temporal domain. Otherwise the wave signal is overlayed by an interfering signal with high-amplitude and long wave length.

The signal of linear surface-gravity waves is well-located on a surface in the wave-number frequency domain defined by the dispersion relation of linear surface-gravity waves [*Young et al., 1985, Seemann, 1997*]:

$$\varpi = \sqrt{gk \tanh kd} + \vec{k} \cdot \vec{u} \tag{5.15}$$

where ϖ indicates the absolute frequency, G the gravitational acceleration, d the water depth, and $\vec{u}$ the velocity of encounter, which is a sum of the platform velocity and the near surface current velocity. The so-called dispersion shell connects the wave numbers k with their corresponding frequency coordinate ω. This function is used for a pre-selection of the Fourier coefficients in the 3-D wave spectrum

of a multi-modal wave field with image features that are not resulting from ocean surface waves:

$$\hat{\eta}_W(\vec{k}, \omega) = \delta(\omega - \varpi(\vec{k}; \vec{u}, d)) \, \hat{\eta}(\vec{k}, \omega). \tag{5.16}$$

As indicated by the δ-function, the water depth d and the velocity of encounter $\vec{u}$ have to be determined for using the dispersion relation as filter. This is done by fitting the theoretical dispersion relation to the signal coordinates in the wave-number frequency spectrum [*Senet et al., 2001, Outzen, 1998*].

To suppress those Fourier coefficients with small wave numbers and those with noise from non-relevant spectral components additionally a bandpass filter is applied. This is performed by a normalized 3-D Gabor filter, which has the advantage of reducing the filtering effects in temporal and spatial domain. A certain wave-number and frequency range around the peak wave number k_0 and peak frequency ω_0 is selected using a Gaussian function:

$$\hat{\Omega}(k_x, k_y, \omega) = e^{-\pi(|k_x - k_{x0}|^2 \sigma_{k_x} + |k_y - k_{y0}|^2 \sigma_{k_y} + |\omega - \omega_0|^2 \sigma_\omega)} \tag{5.17}$$

where σ_{k_x}, σ_{k_y} and σ_ω are the standard deviations that define the filter bandwidth in the corresponding dimensions. The filter is similar to a windowed Fourier transformation with the Gaussian function as window function. In case there are several overlapping wave systems, a segmentation has to be performed. This can be done by applying the 3-D Gabor filter to every significant peak in the spectrum of the dominating wave systems.

The 3-D Gabor filter is multiplied with the complex Fourier coefficients of the wave-number frequency spectrum:

$$\hat{\eta}'_W(\vec{k}, \omega) = \hat{\Omega}(k_x, k_y, \omega) \cdot \hat{\eta}_W(\vec{k}, \omega). \tag{5.18}$$

The remaining spectrum consists only of the harmonics related to the linear surface gravity waves as indicated in Fig. 5.9.

To retrieve the wave field $\eta(\vec{r}, t)$ the 3-D wave spectrum $\hat{\eta}'_W(\vec{k}, \omega)$ is transformed in to the spatial-temporal domain by an inverse 3-D FFT. Fig. 5.10 shows one resulting ocean surface elevation image of the sequence of 32 images, recorded on June 3rd, 2001 at Ekofisk 2/4k. Determining the significant wave height from this image gives $H_S = 4.46$ m which is in good agreement with $H_S = 4.86$ m, retrieved from a co-located time series, recorded by the wave rider buoy.

5.5   Validation

This section is focused on the statistical and deterministic comparison of the ocean surface image sequences, retrieved by the method introduced in this paper, with the co-located measurements of three in-situ sensors, one wave rider buoy and two
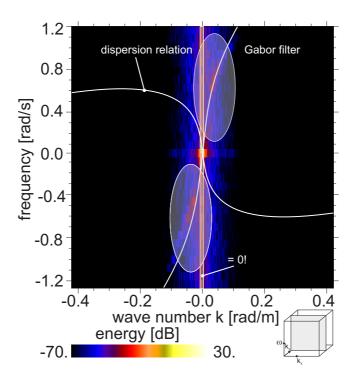
Figure 5.9: Cut through the wave-number frequency spectrum (squared modulus). The signal of the linear ocean surface waves, located on the dispersion relation, is visible. Additionally the Gabor filter is shown, to suppress the small wave numbers (vertical lines) and spectral noise components.
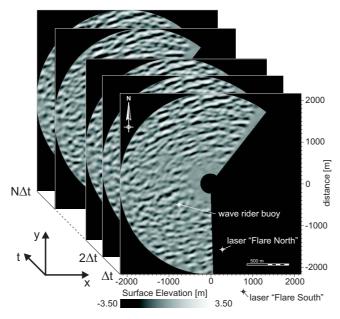

Figure 5.10: Ocean surface elevation sequence of the radar-image sequence recorded on June 3rd, 2001 at Ekofisk 2/4k (see Fig. 5.2). The determined H_S from this image is 4.46 m compared to $H_S = 4.86$ m retrieved from a co-located time series from the wave rider buoy.

laser sensors, which are installed within the measurement area of the radar. The direct deterministic comparison of an ocean surface elevation time series from the radar images and from the buoy gives an impression of the capabilities of this method. Furthermore, a spectral comparison is performed.

5.5.1 Statistical comparison to in-situ data

The significant wave height H_S is the most important quantity used describing a sea state. H_S is used for evaluating the impact of waves and breakers onto watercraft, breakwaters or harbor constructions, in the open sea and coastal zones. It is usually determined directly from a wave record in a number of ways. For the given ocean wave field image sequence $\eta(\vec{r}, t)$, retrieved from radar-image sequences, H_S is directly determined from the standard deviation of the spatial-temporal wave elevation:

$$
\begin{aligned}
H_{S,radar} &= 4 \cdot \left\langle (\eta(r, \phi, t) - \overline{\eta})^2 \right\rangle^{\frac{1}{2}} \\
&\forall \, |\phi - (\phi_W \pm 180°)| \leq 22.5°,
\end{aligned}
\tag{5.19}
$$

where $\overline{\eta}$ gives the population mean, and $\langle \cdot \rangle$ denotes the expectation value of η. Because the radar is mainly imaging waves which travel towards and away from the radar, the significant wave height is determined only for the area within $\pm 22.5°$ of the wave travel direction $\phi_W \pm 180°$.

For comparison, co-located 2 Hz time series of 20 minutes each from the 3 in-situ sensors, one wave rider buoy and two laser sensors ("Flare North" and "Flare South"), are used. The location of all sensors is indicated in Fig. 5.10. Two sensors, the buoy and laser "Flare North", are within the radar measuring range. The buoy is located within the sea surface area visible by the radar. For the time series, the significant wave height is:

$$
H_{S,insitu} = 4 \cdot \left\langle (\eta(t) - \overline{\eta})^2 \right\rangle^{\frac{1}{2}}.
\tag{5.20}
$$

In total, 77 radar data sets with significant wave heights up to 6 m are processed, together with their co-located time series from the in-situ sensors. Fig. 5.11 gives an inter-comparison of the H_S values of the 4 sensors. The upper row shows the comparison of H_S from the three in-situ sensors and from the radar. As expected, the best correlation and lowest standard deviation is found between wave rider buoy and laser "Flare North", because they are located within the measuring area of the radar. The lower row of Fig. 5.11 gives an inter-comparison between all three in-situ sensors. It can be seen that the correlation, bias and standard deviation between the in-situ sensors is within the same range as between the in-situ sensors and the radar. Statistically, the accuracy of the determined H_S from the radar-retrieved ocean surface elevation image sequences is within the accuracy
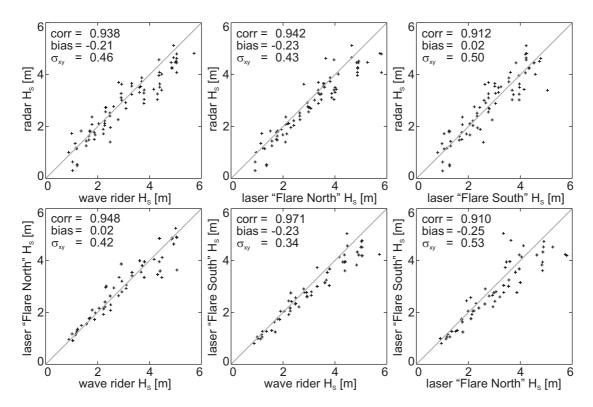
Figure 5.11: Inter-comparison of significant wave heights derived from the inverted radar-image sequences and co-located wave records from three in-situ sensors, a wave rider buoy and the lasers "Flare North" and "Flare South", located in the Ekofisk oil field.

of the in-situ sensors. The radar under-estimates the in-situ values only for small significant wave heights.

5.5.2 Deterministic comparison to in-situ data

Because the wave rider buoy is situated within the line of view of the radar, a direct comparison of the time series of wave elevation, recorded by the buoy $\eta_{buoy}(t)$ and retrieved from the radar-image sequences $\eta_{radar}(\vec{r}_{buoy}, t)$, is possible. The location of the buoy is indicated by $\vec{r}_{buoy}$ and shown in Fig. 5.10. For comparison the radar-image sequence as seen in Fig. 5.2, recorded on June 3rd, 2001, 10:15:00 at Ekofisk 2/4k, has been transformed to the ocean surface elevation image sequence by the introduced inversion method. For this date and the given starting time of the radar record, the co-located buoy time series is taken. With a sampling period of $\Delta t_{radar} = 2.56$ s and 32 images (samples) per radar data set, the total time duration is $T_{tot} \approx 82$ s. The buoy record has a sampling period of $\Delta t_{buoy} = 0.5$ s (2 Hz). Therefore, 164 samples are taken for the given total time duration T_{tot} of the radar data set. The internal clocks of both, radar and buoy system, are not synchronized, but are setup with UTC time. A temporal synchronization procedure between both data sets is therefore necessary. For the analyzed case, the
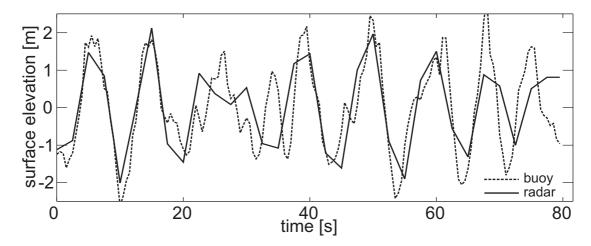
Figure 5.12: Synchronized wave elevation time series derived, respectively, from radar wave elevation time series (solid curve), and a co-located buoy record (dashed curve). The data sets were recorded on June 3rd, 2001, $10:15:00 \pm 1s$ at Ekofisk 2/4k.
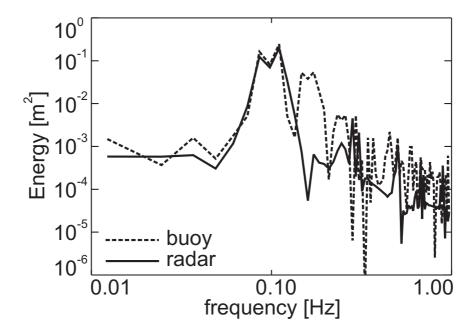

Figure 5.13: Frequency power spectra of the time series of Fig. 5.12.

recorded start time differed by 2 s. Fig. 5.12 shows the overlayed and synchronized time series. The solid curve is the radar-retrieved record at the buoys location and the dashed curve the co-located buoy record. Overall the time series show a good agreement. The amplitudes are within the same range and the periods are the same. There is no phase de-correlation.

This transect in space and time allows the investigation of single wave properties, such as wave height, steepness, etc. Following the zero-up crossing definition for time series, the second wave in the records in Fig. 5.12 is identified as the highest
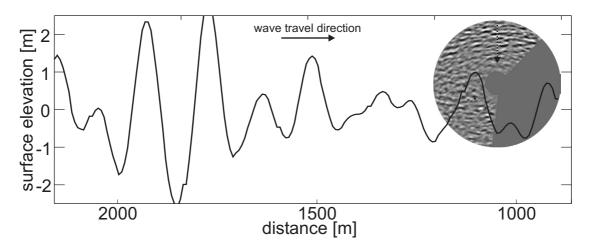
Figure 5.14: Spatial cut through the last of the 32 ocean surface elevation images derived from radar-image sequence, recorded on June 3rd, 2001 at Ekofisk 2/4k. The position and direction of the cut is indicated in the elevation map.

wave with $H \approx 4$ m, beginning at about 10 s. With a wave period of $T \approx 10$ s, the wave steepness ϵ is:

$$\epsilon = H/L \approx 1.56 \cdot H/T^2 = 0.062. \tag{5.21}$$

Fig. 5.13 illustrates the comparison of the frequency energy spectra derived, respectively, from the radar wave elevation map (solid curve), and the buoy record (dashed curve). Both spectra present a good agreement, whereas the radar spectrum is more narrow-banded, due to the band-pass filtering during processing. The peak frequency is in both records at $f_p \approx 0.1$ Hz (10 s), with the same value for the energy maximum.

Fig. 5.14 exemplarily shows a spatial cut through the last of the 32 ocean surface elevation images of the analyzed radar data set. There is a dominant wave group visible travelling southwards. The highest wave, which is found within the group, has a wave height of $H \approx 5$ m. The wave length is $L \approx 180$ m, and the steepness $\epsilon = H/L = 0.028$. Wave groups play an important role for the design and assessment of offshore-platforms, breakwaters or ships, because successive large single wave crests or deep troughs can cause severe damages due to their impact, or they can excite the resonant frequencies of the structures. For ships, an encounter with wave groups can sometimes cause capsize or severe damage. Therefore the detection of wave groups in space and time is of extreme importance for ocean engineers and scientists. For a detailed work on retrieval and investigations of the properties of individual spatial-temporal wave groups from ocean surface elevation image sequences, the reader is referred to [*Dankert et al., 2003a*].

5.6 Conclusions

The empirical inversion method introduced here allows the derivation of sequences of ocean surface elevation maps from radar-image sequences. The inversion scheme is based on the determination of the tilt angle at each pixel of the radar images. The radar images are acquired using a conventional nautical radar. The method represents an extension of the existing techniques for deriving wave spectra and sea state parameters and is seen as an alternative to the inversion scheme as proposed by *Borge et al., 2003*. Different from *Borge et al., 2003* the radar system does not need in-situ sensors. A calibration procedure is not necessary.

The inversion scheme was applied to radar data sets, recorded by the WaMoS system from a platform in the Ekofisk oil field in the central North Sea. For validation of the method, co-located measurements from three in-situ sensors, one wave rider buoy and two laser sensors, were taken. In a first validation phase a statistical wave parameter, the significant wave height, has been determined from the radar-derived time series of ocean surface elevation maps and compared to the significant wave height from co-located in-situ wave records. Furthermore, an inter-comparison between all four sensors has been performed. Thereby correlation, bias and standard deviation between the in-situ sensors is within the same range as between the in-situ sensors and the radar. Therefore, it could be shown, that the accuracy of the radar-retrieved ocean surface elevation image sequences is within the accuracy of the in-situ sensors. The radar under-estimates the in-situ values only for small significant wave heights.

A wave profile measured by the buoy was compared to the co-located radar-derived ocean surface at the location of the buoy. The shown transects in space and time demonstrated the capabilities of the inversion method for studying single wave properties, such as wave height or wave steepness, spatially and temporally. Furthermore, wave groups are detectable and investigatable in space and time from the radar-derived time series of ocean surface elevation maps, which has previously been done in *Dankert et al., 2003a*.

Acknowledgements

Bibliography

Alpers, W. and Hasselmann, K. (1978). The two-frequency microwave technique for measuring ocean wave spectra from an airplane or satellite. *Boundary Layer Metereol.*, 13, 215–230.

Alpers, W. and Hasselmann, K. (1982). Spectral signal to clutter and thermal noise properties of ocean wave imaging synthetic aperture radars. *Int. J. Rem. Sens.*, 3, 423–446.

Alpers, W. R., Ross, D. B., and Rufenach, C. L. (1981). On the detectability of ocean surface waves by real and synthetic aperture radar. *J. Geophys. Res.*, 86, 6 481–6 498.

Bass, F. and Fuks, I. (1979). Wave Scattering from Statistically Rough Surfaces. *Pergamon Press.*

Bell, P. (1999). Shallow water bathymetry derived from an analysis of x-band marine radar images of waves. *Coastal Eng.*, 37, 513–527.

Borge, J. N., Hessner, K., and Reichert, K. (1999). Estimation of the significant wave height with x-band nautical radars. In *Proc. 18th Intern. Conf. on Offshore Mech. and Arctic Eng. (OMAE)*, number OMAE99/OSU-3063 St. John's, Newfoundland, Canada.

Borge, J. N., Rodríguez, G., Hessner, K., and González, P. (in press 2003). Inversion of nautical radar images for surface wave analysis. *J. Atmos. and Ocean Tech.*

Dankert, H. (2003). Retrieval of surface-current fields and bathymetries using radar-image sequences. *Proc. Int. Geosci. Remote Sens. Symp.*

Dankert, H., Horstmann, J., Lehner, S., and Rosenthal, W. (2003a). Detection of wave groups in SAR images and radar-image sequences. *IEEE Trans. Geosci. Remote Sens.*, 41(6), 1 437–1 446.

Dankert, H., Horstmann, J., and Rosenthal, W. (2003b). Ocean wind fields retrieved from radar-image sequences. *J. Geophys. Res.*, 108(C11, 3352, doi: 10.1029/2003JC002056).

Hara, T. and Plant, W. J. (1994). Hydrodynamic modulation of short wind-wave spectra by long waves and its measurement using microwave backscatter. *J. Geophys. Res.*, 99, 9 767–9 784.

Moore, R. (1985). Radar sensing of the ocean. *IEEE J. Oceanic Eng.*, 10, 84–112.

Outzen, O. (1998). Bestimmung der Wassertiefe und der oberflächennahen Strömung mit einem nautischen Radar. In *Diploma Thesis, GKSS Report 98/E/60 (in German)* University of Hamburg, Germany.

Plant, W. (1991). The variance of the normalized radar cross section of the sea. *J. Geophys. Res.*, 96, 20 643–20 654.

Romeiser, R. and Alpers, W. (1997). An improved composite surface model for the radar backscattering cross section of the ocean surface 2. Model response to surface roughness variations and the radar imaging of underwater bottom topography. *J. Geophys. Res.*, 102, 25 251–25 267.

Romeiser, R., Alpers, W., and Wismann, V. (1997). An improved composite surface model for the radar backscattering cross section of the ocean surface 1. Theory of the model and optimization/validation by scatterometer data. *J. Geophys. Res.*, 102, 25 237–25 250.

Romeiser, R., Schmidt, A., and Alpers, W. (1994). A three-scale composite surface model for the ocean wave - radar modulation transfer function. *J. Geophys. Res.*, 99, 9 785–9 801.

Seemann, J. (1997). Interpretation der Struktur des Wellenzahl-Frequenzspektrums von Radar-Bildsequenzen des Seegangs. In *Dissertation, GKSS Report 97/E/68 (in German)* University of Hamburg, Germany.

Senet, C., Seemann, J., and Ziemer, F. (2001). The near-surface current velocity determined from image sequences of the sea surface. *IEEE Trans. Geosci. Remote Sens.*, 39, 492–505.

Shyu, J.-H. and Phillips, O. (1990). The blockage of gravity and capillary waves by longer waves and currents. *J. Fluid. Mech.*, 217, 115–141.

Smith, J. (1990). *Surface waves and fluxes*, chapter Modulation of short wind waves, (pp. 247–284). Kluwer Academics.

Trizna, D. (2001). Errors in bathymetric retrievals using linear dispersion in 3-d fft analysis of marine radar ocean wave imagery. *IEEE Transactions on Geoscience and Remote Sensing*, 39, 2465–2469.

Wetzel, L. (1990). Electromagnetic scattering from the sea at low grazing angles. *Surface Waves and Fluxes, Geernaert and W.J. Plant (eds.), Kluwer Academic Publishers*, II, 109–171.

Wright, J. and Keller, W. (1980). Ocean-wave modulation transfer functions from the West Coast experiment. *Geophys. Res. Lett.*, 85, 4 957–4 966.

Wright, J. W. (1968). A new model for sea clutter. *IEEE Trans. Antennas Propag.*, AP-16, 217–223.

Young, I., Rosenthal, W., and Ziemer, F. (1985). A threedimensional analysis of marine radar images for the determination of ocean wave directionality and surface currents. *J. Geophys. Res.*, 90,C1, 1049–1059.

Ziemer, F. (1995). An instrument for the survey of the directionality of the ocean wave field. In *Proc. of the WMO/IOC Workshop on Oper. Ocean Mon. Using Surface Based Radars*, volume 32 (pp. 81–87). Geneva, Swiss.

Chapter 6

Outlook

The three algorithms, developed within the framework of the European projects MAXWAVE and ENVOC, and introduced in this thesis allow for the first time the retrieval of the ocean surface without calibration, wave groups and wind fields from nautical X-band radar-image sequences with high spatial and temporal resolution.

Individual wave groups have been investigated in SAR images and inverted nautical radar-image sequences [*Dankert et al., 2003b*]. Within the SAR images, with the capability of covering large areas of the ocean surface, it could be shown, that they are not randomly distributed over the ocean. They show preferred travel directions. This phenomenon has to be further investigated for understanding the spatial behavior of wave groups on a global scale. Using inverted nautical radar-image sequences, wave groups have been investigated on a local spatial and temporal scale [*Dankert et al., 2003b*]. Thereby it could be found out, that the group velocity is oscillating and the energy is also transferred along the wave crest. The physics behind this phenomenon will be further investigated. *Dankert et al., 2003a* has shown that the gravity centers of the spatial-temporal wave groups converges and diverges periodically over time. They found that this behavior could be a reason for parametric rolling of ships. Parametric rolling is an unstable phenomenon, which can quickly generate large roll angles that are coupled with significant pitch motions. The rolling occurs in phase with pitch, and on containerships induces high loads into the containers and their securing systems. This is an important issue considering the large number of these vessels. The further investigation of this phenomenon, additionally with radar-image sequences, is therefore a big challenge in the future.

The retrieval of high-resolution wind fields for their investigation was demonstrated [*Dankert et al., 2003d*]. By taking the air-sea temperature difference into account, which describes the dependency of the radar cross section (RCS) on the stability in the lower marine atmospheric boundary layer, a significant improvement of the wind speed retrieval was achieved. Future investiga-

tions aim increasing the measurable wind-speed range and finding the limitations of the method. For this purpose more data sets under a larger bandwidth of weather conditions will be considered. Nevertheless, former studies of *Hatten et al., 1998, Hatten et al., 2003* could show that for wind speeds up to $23\,ms^{-1}$ no saturation in the RCS occurs.

A new method for the retrieval of spatial and temporal varying wind fields was recently introduced by *Dankert et al., 2003c*. This method is based on the idea that with a gliding temporal integration window the static wind streak patterns become both, spatially and temporally, variable. From these variable wind streaks the wind vector is retrieved locally, both spatially and temporally. The local wind vector at each point in the investigated area is determined using tensor-based techniques [*Jähne et al., 1999*]. With this technique wind fields can be investigated spatially and temporally and no calibration of the images or training of a NN is necessary. The method is recently investigated.

The introduced inversion scheme for the spatial and temporal determination of the ocean surface has been demonstrated as a powerful method [*Dankert and Rosenthal, 2003*]. No additional calibration information from in-situ sensors are necessary. The WaMoS system can operate now as stand-alone instrument. Further investigations using nautical radar-image sequences from different platforms and ships have to be performed to find its limitations.

Catastrophes due to incidences of rogue waves, which are individual waves of exceptional height or steepness, at off-shore platforms and ships were reported by *Kjeldsen, 1996*. Several incidences of impacts of rogue waves onto ships with heavy damage are documented [*Faulkner and Buckley, 1997*]. With long-term radar observations, both occurring rogue waves and the given wind field, can be recorded spatially and temporally. Studies on the shape, the occurrence probability of rogue waves and the environmental condition, which caused such a wave, can be performed. Information about an approaching extreme wave will help mariners starting emergency procedures in sufficient time. Some of the documented catastrophes might have been prevented using the invented methods.

All methods introduced in this thesis are based on nautical X-band radar-image sequences. They offer a unique opportunity for a combined monitoring and investigation of wind and waves on a long-term basis. The investigation of both, wind and waves, in spatial-temporal dimensions will help to better understand the processes between the upper ocean surface and the lower marine atmospheric boundary layer. The combination of the presented wave and wind field retrieval techniques will provide additional information on both ocean waves, wind fields and the atmosphere ocean interface. The combined spatial-temporal wind-wave information will help engineers to improve and simplify the procedures for the designing of maritime structures against random ocean waves and winds. A WaMoS installed aboard a ship will be permanently provided with important information

about the surrounding wind-wave conditions.

In 2005 the satellite TerraSAR-X, equipped with a SAR, is scheduled to be launched. The Wide Swath Ocean Altimeter (WSOA) is also planned to be launched in the near future. This altimeter is based on the technique of radar interferometry. Both satellites will be able to map and study the ocean surface on a global scale, like the already flown ERS-1,2, and ENVISAT satellites. An important task is the calibration of these satellite-based radar images. WaMoS data, inverted by the new method, which was introduced in this thesis (cf. chapter 5), can significantly contribute to this calibration process. The WaMoS system is thereby one of the few available calibration tools.

Bibliography

Dankert, H., Horstmann, J., Günther, H., and Rosenthal, W. (in press 2003a). Measurements of wave groups using radar-image sequences. *Elsevier Oceanography Series.*

Dankert, H., Horstmann, J., Lehner, S., and Rosenthal, W. (2003b). Detection of wave groups in SAR images and radar-image sequences. *IEEE Trans. Geosci. Remote Sens.*, 41(6), 1 437–1 446.

Dankert, H., Horstmann, J., Magnusson, A., and Rosenthal, W. (2003c). Ocean winds retrieved from x-band radar-image sequences. *Proc. Int. Geosci. Remote Sens. Symp.*

Dankert, H., Horstmann, J., and Rosenthal, W. (2003d). Ocean wind fields retrieved from radar-image sequences. *J. Geophys. Res.*, 108(C11, 3352, doi: 10.1029/2003JC002056).

Dankert, H. and Rosenthal, W. (submitted 2003). Ocean surface determination from x-band radar-image sequences. *J. Geophys. Res.*

Faulkner, D. and Buckley, W. (1997). Critical survival conditions for ship design. In *RINA Int. Conf.* (pp. 1–41). Glasgow, Scotland.

Hatten, H., Seemann, J., Horstmann, J., Senet, C., and Ziemer, F. (submitted 2003). Azimuthal and range dependency of sea-surface radar backscatter at hh-polarization and low grazing incidence. *IEEE Trans. Geosci. Remote Sens.*

Hatten, H., Ziemer, F., and Nieto-Borge, J. S. J. (1998). Correlation between the spectral background noise of a nautical radar and the wind vector. *Proc. 17th Intern. Conf. on Offshore Mech. and Arctic Eng. (OMAE).*

Jähne, B., Haußecker, H., and Geißler, P. (1999). *Handbook of Computer Vision and Applications.* Academic Press.

Kjeldsen, S. (1996). Example of heavy weather damage caused by giant waves. *Bul. Soc. Nav. Arch. Japan*, 820.

Acknowledgements